

Article

Robust Speed Control of a Multi-Mass System: Analytical Tuning and Sensitivity Analysis

Muhammed Alhanouti * and Frank Gauterin 

Institute of Vehicle System Technology, Karlsruhe Institute of Technology, 76131 Karlsruhe, Germany;
frank.gauterin@kit.edu

* Correspondence: m.hanouti@gmail.com; Tel.: +49-176-4587-7505

Abstract: The regeneration of highly dynamic driving maneuvers on vehicle test benches is challenging due to several influences, such as power losses, vibrations in the overall system that involves the vehicle with the test bench, uncertainties in the model parameterization, and time delays from both the test bench and the measurement systems. In order to improve the dynamic response of the vehicle test bench and to overcome system disturbances, we employed different types of control algorithms for a mechanical multi-mass model. First, those controllers are extensively investigated in the frequency domain to analyze their stability and evaluate the noise rejection quality. Then, the expectations from the frequency analysis are confirmed in a time-domain simulation. Furthermore, sensitivity analysis tests were conducted to evaluate each controller's robustness against the modeling parameters' uncertainty. The linear quadratic controller with integral action demonstrated the best compromise between performance and robustness.

Keywords: test bench; electric vehicle; multi-mass system; linear quadratic state-space controller; robust control; vibration suppression; frequency analysis; sensitivity analysis



Citation: Alhanouti, M.; Gauterin, F. Robust Speed Control of a Multi-Mass System: Analytical Tuning and Sensitivity Analysis. *Appl. Sci.* **2023**, *13*, 13268. <https://doi.org/10.3390/app132413268>

Academic Editor: Suchao Xie

Received: 9 November 2023

Revised: 7 December 2023

Accepted: 11 December 2023

Published: 15 December 2023



Copyright: © 2023 by the authors. Licensee MDPI, Basel, Switzerland. This article is an open access article distributed under the terms and conditions of the Creative Commons Attribution (CC BY) license (<https://creativecommons.org/licenses/by/4.0/>).

1. Introduction

The powertrain test benches apply the desired driving resistances directly to the wheel-hub of the test vehicle. So, the loading machines will be coupled to the vehicle's powertrain [1,2]. This setup establishes high stability and allows the powertrain to operate without restraint while the wheel-hubs are attached to electrical load machines [3]. Therefore, powertrain test benches are practical tools for highly dynamic driving condition simulation and advanced driving assistance systems applications. For instance, in [1,2], a control concept for powertrain test benches was proposed to simulate different street conditions, such as dry, wet, or icy. The reliability of this concept was proved by successfully simulating the anti-lock braking system performance on the road with a side ice patch. Nevertheless, accurate tire modeling becomes indispensable to compensate for the absence of the actual tire characteristics. For example, an approach was proposed to establish a correlation between the road and the test bench measurements in [4]. The developed method is based on empirically optimizing the Pacejka tire model parameters.

The complete vehicle test benches are developed to allow the steering of the front wheels and even vertical excitation. These assets contribute to bridging the gap between real-world driving and vehicle-in-the-loop (VHiL) simulation. In addition, the complete vehicle test benches took the VHiL-testing to a new level by enabling more degrees of freedom in automotive testing. In addition to the four electrical loading machines used in the powertrain test benches, the complete vehicle test benches have actuators on the steering wheels to simulate the self-aligning torque phenomenon [5].

Many researchers used a proportional-integral-controller (PI) to reduce the unwanted dynamics in mechanical torsional systems [6,7]. The widely spread utilization of the PI controller is due to its simple design and tuning techniques, its ability to be adapted to many

applications, and its lack of an SS model [8,9]. However, the performance of the PI control is inferior to the other control algorithms, such as SS feedback control [8,9]. Furthermore, only a single design goal can be optimally solved. For instance, a PI controller can be tuned for high robustness or quick signal tracking performance, but not both [8,10,11]. In addition, many studies proved that PI control could not effectively dampen the torsional vibrations [10,12,13]. Moreover, since it has only two tunable parameters (i.e., proportional gain (k_p) and integral gain (k_i)), it has limited performance with high-order systems [8,10]. In contrast, SS feedback control allows placing the closed-loop poles anywhere in the space [10]. The limitations of the PI controller were further investigated in [10,14]. One of the techniques to compensate for the limited number of closed-loop poles of the PI controller is implemented by adding more internal feedback to the system control loop. The authors of [15] conducted a study for employing a double feedback coefficient pole placement to improve two-inertia system performance. Based on a proper choice for the location of the closed-loop system poles, different cases were investigated for the poles of a cascade control structure with a PI speed controller. System dynamics were investigated for different natural angular frequencies and damping coefficients (i.e., different closed-loop poles). Likewise, two additional feedback gains are employed in [16]: one is for the shaft moment, and the second is for the angular speed difference between the motor and the wheel.

A more efficient approach for vibration suppression is achieved with feedback gains from all system state variables, namely, shafts' torsional moment and the corresponding rotational speed of each inertia. The SS control realizes this concept [17–19]. SS control gained its advantage from its features that support the control process. According to [8], the fundamental feature of SS control is that it enables fast detection of deviations in all system states because it allows information from the internal states of the plant. In addition, it has a structured design procedure that makes high-control performance achievable. Furthermore, with SS representation, nonlinearities in the model become easier to handle. Nevertheless, it was also highlighted in [8,13] that SS control has downsides. For instance, it does require thorough SS modeling. The second disadvantage is that the designing controller parameters are not directly interpretable. As a consequence, high implementation and tuning efforts are likely. Also, compared to the PI controller, it has a more complex design approach. Moreover, the steady-state accuracy is only apparent since the parameters are uncertain. Finally, and most importantly, it cannot regulate the output error.

In order to overcome the inadequacy of SS control in compensating for the output error, a synthesized controller from SS control algorithms with the additional integral yield is suggested. The additional integral yields the closed-loop output to converge to zero steady-state error when the desired value is constant. This type of control is called state-space feedback with integral action (I-SS). More details about I-SS control can be found in [8,10,20]. It was also proven in [10] that the state-space feedback controller with the additional integral is a much better choice than the PI controller with additional feedback. Nevertheless, the modification of SS to I-SS control is made at the expense of increasing the settling time and reducing the phase margin compared to SS control. An investigation of the performance of different control algorithms, namely, the conventional PI control, I-SS control, and model predictive control (MPC), is performed [13]. The results showed that the PI ranked the lowest in the criterion of dynamic characteristics. In contrast, both I-SS and MPC achieved better results at the expense of higher complexity of implementation and tuning. Furthermore, regarding stability and robustness, I-SS was at the top of the list, followed by PI, while MPC came last. Finally, the MPC entailed the highest calculation effort in terms of processing time. It is concluded from this thorough study that the decision of the best speed control method depends on the user and the type of application. Among all the previously mentioned references, the authors of [7,11] have developed an SS controller for a multi-mass system, while the rest had applications with a two-mass system at the most. Thus, an I-SS controller for a multi-mass system will be proposed in this work. Furthermore, an optimized PI and SS controller, similar to the control algorithm in [11],

will be developed. Then, an extensive analysis of all controllers will be performed to define the limits of implementing each controller type. The analysis will comprise the theoretical equations, frequency response, time-domain response, and sensitivity analysis.

An essential area that, unfortunately, did not receive enough attention from researchers is the need for a robust control algorithm for the combined system of the test bench and the test vehicle's powertrain. So, this research conducts an in-depth investigation of the development of a control algorithm for high-performance powertrain test benches'. In Section 2, a multi-mass model for the integrated system from the powertrain of the test vehicle and the mechanical part of a complete vehicle test bench is derived. The developed model will be employed in Section 3 to create different angular speed control algorithms. Frequency analysis and the measurement's noise-amplification are performed on all controllers to evaluate their robustness. A time-domain response investigation of the control alternatives is conducted in Section 4. The evaluation criteria of the different controllers are mainly based on performance, robustness, and sensitivity analysis.

2. System Modeling

Figure 1 shows the layout of a testing platform called the VEHICLE-in-the-Loop (VEL). The primary purpose behind the VEL test bench is to regenerate the driving environment influences, resembled by driving resistances on the tires. The wheel hub adaptation enables the direct connection of the VEL to the vehicle's wheel hub. The VEL test bench comprises two types of actuators: four electrical loading machines labeled as (1) in Figure 1. These loading machines are powered with electrical inverters, labeled as (4). The main task of these motors is to regenerate the driving resistances of the assigned driving maneuver around the spinning axis of the wheel. The second type of actuator is the two servo motors, labeled as (2) in Figure 1. These actuators permit the simulation of the self-aligning torque at the front wheels. Moreover, environment wind speed is simulated with the airstream simulator, marked as (3) in Figure 1.

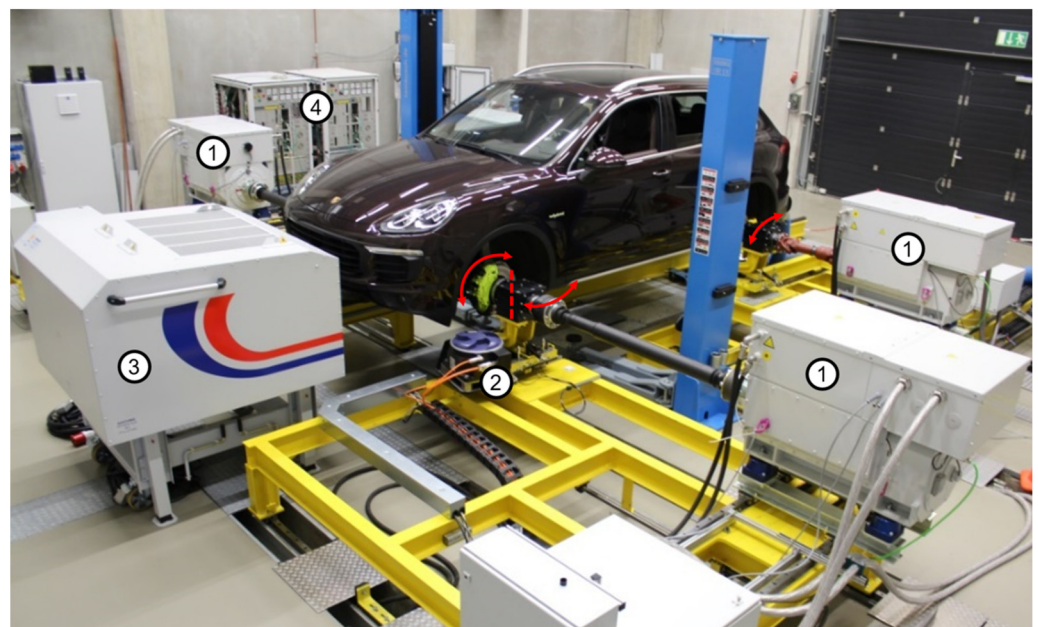


Figure 1. VEHICLE-in-the-Loop. <https://www.fast.kit.edu/lff/4667.php>, accessed on 18 March 2023.

Thus, straight and curved driving tests can be realized inside the lab room. Furthermore, the track width and wheelbase setting enable many vehicles with different geometrical dimensions to be accommodated [21]. The technical data of the VEL test bench are listed in Table 1.

Table 1. Technical specification data of VEL test rig.

Feature	Value
Maximum allowable vehicle mass	12,000 [kg]
Maximum allowable wheel load	3000 [kg]
Wheelbase range	1.8–4.9 [m]
Vehicle's track width range	1.2–3.9 [m]
Maximum loading machine speed	2000 [RPM]
Nominal loading machine torque	2500 [N.m]
Nominal loading machine power	209 [kW]
Steering angle range at the front wheels	±20 [degree]
Maximum steering load torque at the front wheels	1000 [N.m]
Maximum air speed of the portable airstream simulator	135 [km/h]

2.1. Modeling of VEL Test Rig

The system plant consists mainly of the vehicle under the test powertrain, which is, in this case, a front-wheel-drive electric vehicle. A constant velocity (CV) shaft connects each loading machine with the powertrain's corresponding axle and wheel hub. The installed measurement devices are an angular speed sensor at each loading machine end and a moment sensor at each wheel-hub end.

The resistance moments generated by the electric loading machines are delivered to the wheel hub through the power transmission of the VEL, as illustrated in Figure 2. Since the right and left sides of the front-drive system with the VEL test bench are symmetric, a reduced system of half of the total system may be considered for building the model equations. Then, a suitable control algorithm is developed based on that. Finally, the complete system (i.e., full plant and the developed controllers for both sides) is used for testing. Similar approaches are considered in [11,22,23]. As shown in Figure 3, the plant can be modeled as three masses and two spring-damper systems.

The three masses are the loading machine plus the CV shaft inertia (J_T), the wheel-hub inertia (J_W), one axle inertia plus half of the powertrain equivalent inertia (J_{Pt2W}). The two spring-damper systems are CV shaft-equivalent torsional spring and damper coefficients and the axle-equivalent torsional spring and damper coefficients. Due to the relative flexibility of the shaft between the loading machine and the wheel hub, the shafts will be respected as flexible coupling components with equivalent stiffness and internal damping. The system has two inputs: first, the resistance moment from the loading machine (M_M), which will be the manipulated variable for the speed controller; and second, half of the final moment at the differential output gear (M_{5x}) (i.e., $x = \text{left, right}$). One output state variable is assigned for the system, which is the measured angular speed of the loading machine. The gearboxes of modern commercial vehicles are produced with high efficiency, so backlash losses become negligible [23,24]. The friction influence between gears is indeed significant. Including friction in the system's equations adds nonlinear dynamic constraints to the model, making the system more stable [25]. The friction acting in the differential gearbox combines Coulomb and viscous friction [11,23,24]. The Coulomb friction moment has a constant value (M_{F0}) and a moment-dependent part. The total output moment from the differential equals the vehicle's motor moment (M_e) multiplied by the total gear transmission ratio (i.e., gearbox transmission ratio (i_g) multiplied by the differential transmission ratio (i_d)). This last quantity is specified by the factor (k_M). The factor ($k_{\Delta\omega}$) and the angular speed difference between the differential outputs ($\Delta\omega_D$) determine the viscous friction moment portion. Therefore, the total gear friction moment (M_F), which can be considered a disturbance, is described in Equation (1) [24]

$$M_F = (M_{F0}i_d + k_M|M_ei_gi_d|)sgn(\Delta\omega_D) + k_{\Delta\omega}\Delta\omega_D \quad (1)$$

M_F will be distributed equally between the left and right sides of the total system model [23,24]. The parameterization of the mechanical part of VEL associated with the front wheels is listed in Table 2. The controlled system plant and the controller in the state

space can be described in differential equations and in the form of matrices. Therefore, Equation (2) describes the three-mass system shown in Figure 3

$$\begin{aligned}
 J_T \frac{d\omega_M}{dt} &= M_M - D_S(\omega_M - \omega_W) - K_S(\theta_M - \theta_W) \\
 J_W \frac{d\omega_W}{dt} &= D_S(\omega_M - \omega_W) + K_S(\theta_M - \theta_W) - D_{Ax}(\omega_W - \omega_{Sx}) - K_{Ax}(\theta_W - \theta_{Sx}) \\
 J_{Pt2W} \frac{d\omega_D}{dt} &= D_{Ax}(\omega_W - \omega_D) + K_{Ax}(\theta_W - \theta_D) - M_{Sx} - \frac{M_F}{2}
 \end{aligned} \tag{2}$$

where $J_{Pt2W} = J_A + \frac{J_D i_d^2 + (J_E + J_g) i_g^2}{2}$.

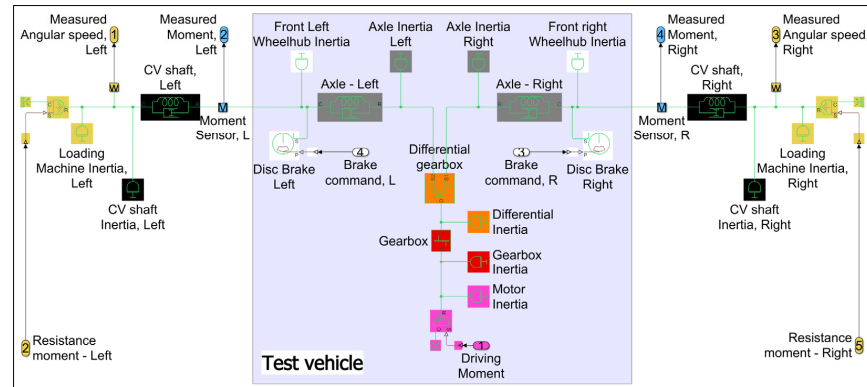


Figure 2. Complete simulation model of VEL mechanical power transmission system and a front-wheel-drive.

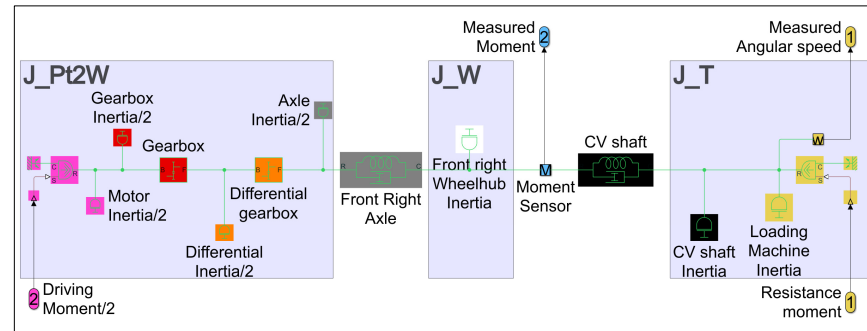


Figure 3. Three mass models.

Table 2. Parameters of the VEL mechanical parts associated with front wheels.

Element	Value	Unit	References
Powertrain motor inertia (J_E)	0.03	Kg·m ²	[26]
Wheel hub inertia (J_W)	0.124	kg·m ²	[27]
Axle inertia (J_{Ax})	3.7×10^{-4}	kg·m ²	[27]
Differential inertia (J_D)	1×10^{-2}	kg·m ²	[26–28]
Gearbox inertia (J_G)	0.0524	kg·m ²	[27]
Gearbox transmission ratio (i_g)	4	-	Technical data
Differential transmission ratio (i_d)	2.5	-	Technical data
Loading machine inertia (J_M)	0.6	kg·m ²	Technical data
CV shaft inertia (J_S)	0.0243	kg·m ²	Technical data
CV shaft stiffness (K_S)	1715	N.m/rad	Technical data
CV shaft internal damping (D_S)	5.99	N.m.s/rad	Technical data
Axle stiffness (K_{Ax})	7700	N.m/rad	[29]
Axle internal damping (D_{Ax})	3.57	N.m.s/rad	[30]
Coulomb friction constant (M_{F0})	0.5	N.m	[23]
Friction moment factor (k_M)	0.06	-	[23]
Viscous friction factor ($k_{\Delta\omega}$)	0.06	-	[23]

In order to rewrite the model in a state-space (SS) presentation, the state variables need to be specified as follows:

- The angular speed of the electrical loading machine (ω_M);
- The difference between the loading machine angular position (θ_M) and the wheel-hub angular position (θ_W);
- The angular speed of the wheel-hub (ω_W);
- The difference between wheel-hub angular position (θ_W) and the differential gear output angular position (θ_{Sx});
- The angular speed of the differential gear output (ω_{Sx}).

Accordingly, the state vector becomes

$$x^T = [\omega_M \quad (\theta_M - \theta_W) \quad \omega_W \quad (\theta_W - \theta_{Sx}) \quad \omega_{Sx}]$$

where ω_M is the reference variable, ω_W and ω_{Sx} are estimated outputs, and $(\theta_M - \theta_W)$ and $(\theta_W - \theta_D)$ are estimated disturbances. The model is given in matrix form as in Equation (3).

$$\dot{x} = \underbrace{\begin{bmatrix} -\frac{D_S}{J_T} & -\frac{K_S}{J_T} & \frac{D_S}{J_T} & 0 & 0 \\ 1 & 0 & -1 & 0 & 0 \\ \frac{D_S}{J_W} & \frac{K_S}{J_W} & -\frac{(D_S+D_{Ax})}{J_W} & -\frac{K_{Ax}}{J_W} & \frac{D_{Ax}}{J_W} \\ 0 & 0 & 1 & 0 & -1 \\ 0 & 0 & \frac{D_{Ax}}{J_{Pi2W}} & \frac{K_{Ax}}{J_{Pi2W}} & -\frac{D_{Ax}}{J_{Pi2W}} \end{bmatrix}}_A x + \underbrace{\begin{bmatrix} \frac{1}{J_T} \\ 0 \\ 0 \\ 0 \\ 0 \end{bmatrix}}_{B_M} M_M + \underbrace{\begin{bmatrix} 0 \\ 0 \\ 0 \\ 0 \\ -\frac{1}{J_{Pi2W}} \end{bmatrix}}_{B_W} M_{Sx} + \underbrace{\begin{bmatrix} 0 \\ 0 \\ 0 \\ 0 \\ -\frac{1}{2J_{Pi2W}} \end{bmatrix}}_E M_F \quad (3)$$

$$y = \underbrace{\begin{bmatrix} 1 & 0 & 0 & 0 & 0 \end{bmatrix}}_C x.$$

A is the system’s state space matrix, B_M is the input matrix of moment M_M , B_W is the input matrix of moment M_{Sx} , E is the input matrix for the disturbance moment M_F , and C is the output matrix.

2.2. Time Delay Model

An inverter must adjust the electric machines’ voltage supplies to manipulate the electromagnetic moments since the loading machines cannot be controlled directly. The moment control of the loading machines is realized using vector control methods and a designated field-oriented control [23]. The moment control response can be modeled as a transfer function from the reference moment to the actual motor moment [10,31]. According to [23,31], the time delay response in electrical components $G_t(s)$ is modeled as in Equation (4)

$$G_t(s) = e^{-s T_d} \frac{\alpha_t}{s + \alpha_t} \quad (4)$$

where T_d is the time delay in the moment control loop and α_t is the bandwidth of the electrical part of the VEL test bench (i.e., the inverter with the loading machine). If T_d in the moment control loop of the inverter exceeds a certain level, it can lead to instability of the angular speed control loop, particularly if the high resonance frequencies need to be considered [10,23]. Therefore, the hardware setup of the electrical components should be optimized for small time delays and sudden changes at the moment.

Another source of time delay is caused by the angular speed measurement of the electric loading machines, as indicated in [10], typically achieved by an incremental encoder. The working principle of the incremental encoder is based on calculating the difference in the measured rotational angle within a specific sampling time interval. Thus, significant quantization noise and time delays in the measurements are produced from the sampling scheme [32]. Hence, the measurement time delay is modeled in [10] as a transfer function $M(s)$ with a given measurement time delay (T_m). Hence, $M(s)$ model (5) yields

$$M(s) = e^{-T_m s} . \quad (5)$$

In [10], the total delay of the sum of T_d and T_m was examined for a two-mass system. As a result, the total delay transfer function is designated in Equation (6) as (G_Δ)

$$G_\Delta(s) = G_t(s)M(s) = e^{-s(T_d+T_m)} \frac{\alpha t}{s + \alpha t}. \quad (6)$$

3. Development of the Control Algorithm

The system in Figure 3 is accurately modeled as a nonlinear higher-order system of a multi-mass oscillator. However, because of the high complexity of this mathematical model, it will not be suitable for controller design. Hence, the nonlinearities may be ignored when designing the controller. Even so, the nonlinearities should be considered in the simulation [11,23,24].

The three-mass system model has five poles 0, $-2.65 \pm j 108$, and $-41.2 \pm j 1310$, as shown in Figure 4. The pole at 0 makes the system marginally stable. The other poles characterize the plant system's resonance frequencies: 108 rad/s and 1310 rad/s, and the corresponding damping ratios: 0.0244 and 0.0315. The poles 0, $-2.65 \pm j 108$, which demote the original system's stability, are dominant. Obviously, the system requires a control algorithm that makes it more stable and enhances the damping properties. Suppose a shaft with relative flexibility connects the wheel-hub with the loading machine. In that case, a control algorithm is required to compensate for the mechanical losses and suppress the vibrations in the system [2]. These are achieved mainly by manipulating the angular speeds to minimize the twist angle differences between the shaft ends [10–12,14,16]. Other sources of torsional vibrations are the backlash between gears [6,23,33,34] and the moment harmonics from the electrical machines [2,23].

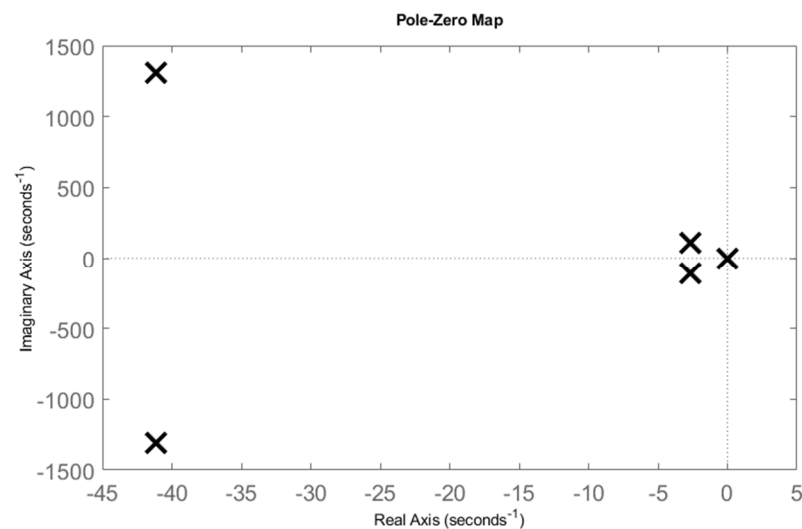


Figure 4. Poles of the system plant.

3.1. Controller Design

The linear-quadratic (LQ) optimization method is implemented to systematically determine the state's feedback gains [8,35,36]. LQ design leads to a more robust controller than the eigenvalue placement gains method [8,35,36]. So, the LQ method will be adopted to design the state feedback gains. The main idea of the LQ optimization approach is to minimize a quadratic cost function (7), with \mathbf{Q} and \mathbf{R} as the weighting matrices for the state vector (\mathbf{x}) and the input vector (\mathbf{u}), respectively. The cost function (J) is minimized by the state feedback controller law (8) and subject to the plant system dynamics. This approach, in contrast to the standard pole placement method, leads to a globally optimal solution for the gain matrix (K_{LQ}). K_{LQ} is determined as in Equation (9), which also depends on the solution (P) of the Riccati Equation (10). A state control loop can easily be implemented with a well-designed system model. Then, the feedback of all state variables creates a

multi-loop control loop [8]. Practically speaking, designing a good-performing SS controller will be challenging if not all the necessary system state variables are measurable, which is a pervasive issue in industrial applications [7,11,13].

Unfortunately, direct feedback from each state variable is often unfeasible since measuring every mechanical variable would be difficult, excessively costly, or reduce the system’s reliability. Hence, advanced estimators of these variables are necessary [18,19,37]. Therefore, estimating the nonmeasurable variables with estimation algorithms, such as the Luenberger observer, neural network, or Kalman filters [35,36], becomes indispensable to solving the problem of nonmeasurable state variables [18,19,37]. In many research studies, Luenberger observers were employed to estimate nonmeasurable state variables. If the system is linear with nonvariant parameters and moderate measurement noises, then the states can be accurately estimated [19].

$$J = \int_0^\infty (x^T Q x + u^T R u) dt \tag{7}$$

$$u = -K_{LQ} x \tag{8}$$

$$K_{LQ} = R^{-1} B_M^T P \tag{9}$$

$$A^T P + P A - P B_M R^{-1} B_M^T P + Q = 0 \tag{10}$$

The Luenberger observer gain matrix (L_{LQ}) is attained by the pole placement method. In order to obtain a high estimation quality, the desired poles are determined from the eigenvalues of the closed-loop characteristics matrix (11) of the full-state feedback controller, and the same method is utilized [11]. Then, the dynamics of the estimated state variables vector (\hat{x}) are determined by Equation (12). By comparing the actual measured output (y) with the estimated output (\hat{y}), \hat{x} is corrected until it matches the actual state variables vector (x). Therefore, the observer’s error dynamics (e) are given in Equation (13)

$$(A_{cl})_{LQ} = \begin{bmatrix} A - B_M K_{LQ} & B_M \\ C & 0 \end{bmatrix} \tag{11}$$

$$\dot{\hat{x}} = A \hat{x} + B_M u + L_{LQ} (y - \hat{y}) \tag{12}$$

$$\dot{e} = \dot{x} - \dot{\hat{x}} = (A - L_{LQ} C) e. \tag{13}$$

So far, the regulator is designed to handle the transient state. However, the steady-state error needs to be handled. Unlike the other control methods, LQ feedbacks all the states multiplied with the designed K_{LQ} , and then compares the final result with the reference signal. A precompensation gain (F) is added to the reference signal as an adjustment. The gain F is determined using Equation (14) [8,35,36].

$$F = \left(C(-A + B K_{LQ})^{-1} B \right)^{-1} \tag{14}$$

We obtain the full LQ controller by assembling the full-state controller with the linear part of the state estimator. Lastly, the obtained closed-loop system is described in Equation (15) [8,35]

$$\dot{\hat{x}} = (A - L_{LQ} C - B_M K_{LQ}) \hat{x} + [F B_M \ L_{LQ}] \begin{bmatrix} y_d \\ y \end{bmatrix} u = -K_{LQ} \hat{x} + F y_d. \tag{15}$$

The block diagram representation of the complete system’s transfer function (16) is illustrated in Figure 5. $G(s)$ is the state-space system’s transfer function, and the transfer

function from the manipulated variable M_M to the output y is given in Equation (17). The regulator transfer function $R(s)$ comprises the state's feedback controller and observer.

$$G(s) = \frac{Y(s)}{M_M(s)} = C(sI - A)^{-1}B_M G_\Delta \tag{16}$$

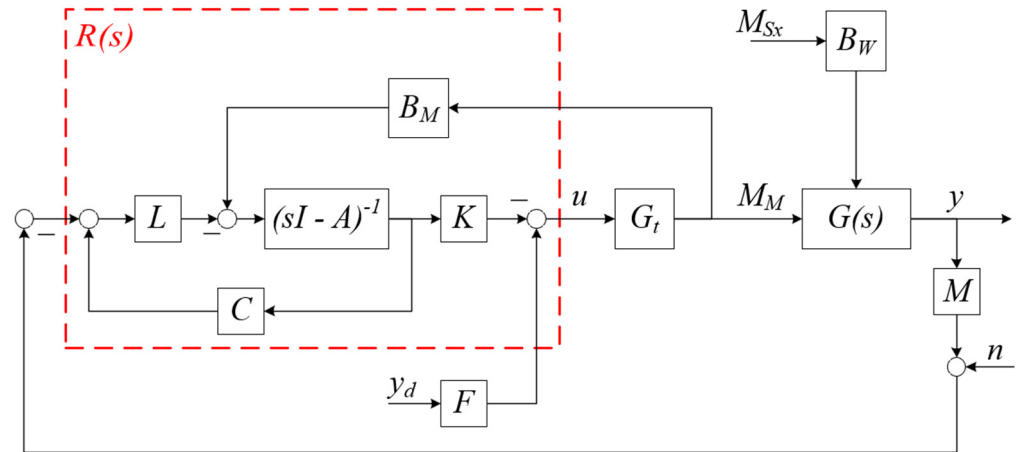


Figure 5. Block diagram of the plant system and the full-state controller.

The closed-loop poles of the LQ-controlled system in Figure 5 cannot be specified directly. According to Equations (9), which also depends on the solution (P) of the Riccati Equation (10), if the weighting matrices Q and R are chosen to be diagonal matrices, each feedback gain in K_{LQ} could be tuned for its corresponding state variable without affecting the feedback gains for the other state variables [8,11]. The tuning of the Q and R is performed iteratively, and the results are shown in Equation (17). The criteria of tuning were minimizing the following: first, the difference between the estimated values of $(\theta_M - \theta_W)$ and $(\theta_W - \theta_{Sx})$, which is crucial in reducing the fluctuations and vibration in the system [11]; second, the steady-state error of y [8,11]; and third, the controller effort by minimizing the manipulated variable M_M , which decreases the stress on the mechanical parts and, at the same time, prevents overloading the electrical components [11,22,23]. With Q and R , K_{LQ} and L_{LQ} are determined as in Equation (18). The value of precompensation gain F is equal to 277. Figure 6 presents upgrading the LQ-controlled system, shown in Figure 5, to the LQ with an integral action (LQI)-controlled system. The LQI controller design is achieved according to [8,10,20]. First, the plant should be redefined with an extended form to include the integral action. After that, feedback should be considered in the controller structure to regulate the output variable through the integrator. Then, all the LQ design theories are applied to LQI.

$$Q = \begin{bmatrix} 1 \times 10^8 & 0 & 0 & 0 & 0 \\ 0 & 1 & 0 & 0 & 0 \\ 0 & 0 & 5 \times 10^6 & 0 & 0 \\ 0 & 0 & 0 & 1 & 0 \\ 0 & 0 & 0 & 0 & 1 \times 10^7 \end{bmatrix}, R = 1500 \tag{17}$$

$$K_{LQ} = [250.75 \quad -1211.20 \quad 12.07 \quad 612.79 \quad 14.07], L_{LQ} = \begin{bmatrix} 401.65 \\ 0.01 \\ 97.35 \\ -0.08 \\ 3.38 \end{bmatrix} \tag{18}$$

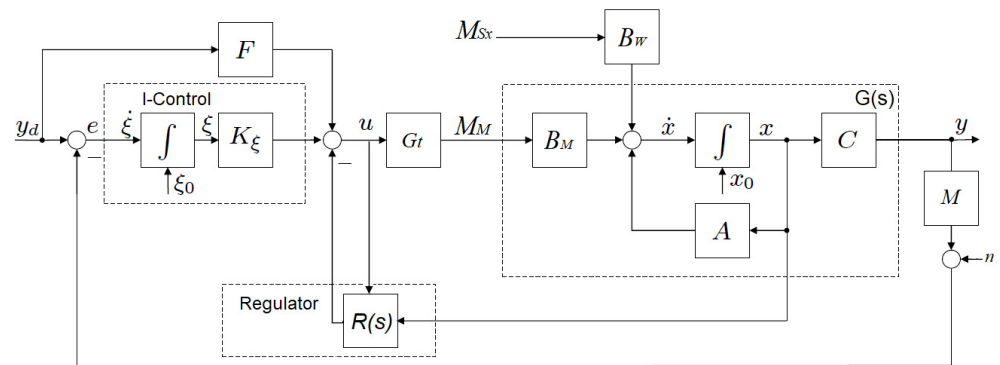


Figure 6. Block diagram representation of the plant system and the I-SS controller.

The first step in the design procedure is to define the error between the measured output and desired output and desired signal as a new state variable (ζ) so that the extended system with the integrator becomes as in Equation (19).

$$\begin{aligned} \dot{\zeta} &= y - y_d \\ u &= -K_x x - K_\zeta \zeta - F y_d \\ \begin{bmatrix} \dot{x} \\ \dot{\zeta} \end{bmatrix} &= \begin{bmatrix} A & 0 \\ C & 0 \end{bmatrix} \begin{bmatrix} x \\ \zeta \end{bmatrix} + \begin{bmatrix} B \\ 0 \end{bmatrix} u + \begin{bmatrix} 0 \\ -1 \end{bmatrix} y_d \\ y &= [C \quad 0] \begin{bmatrix} x \\ \zeta \end{bmatrix} \end{aligned} \tag{19}$$

It was found that using the same tuned values of the weighting matrices Q and R in weighting matrices of LQI , which are Q_i and R_i , will lead to equivalent robustness and control effort to LQ . Of course, an additional tuning effort is made for the last Q_i parameter related to the new state variable (ζ). In addition, the tuning was made with the aim of both LQ and LQI having analogous closed-loop poles so that a reasonable comparison between them could be made. The tuned Q_i and R_i are provided in Equation (20). The gain matrix for LQI (K_{LQI}) and its observer gain matrix (L_{LQI}) are determined similarly for K_{LQ} and L_{LQ} . The results are found in Equation (21). The value of precompensation F gain in the case of LQI is equal to 320.5. Accordingly, the PI controller gains are tuned until the dominant poles of the PI controller system are as close as possible to the LQI controller system. Consequently, the PI controller gains are set to k_p equals 260, and k_i is 2050. With that achieved, it is expected that both systems would have similar time responses. Figure 7 shows the closed-loop poles related to each controller. The LQ -controlled system has 10 stable poles, while employing LQI produced 11 stable poles, and the result with the PI controller is only six stable poles. This observation means that all controllers do not have the zero pole from the original plant.

$$Q_i = \begin{bmatrix} 1 \times 10^8 & 0 & 0 & 0 & 0 & 0 \\ 0 & 1 & 0 & 0 & 0 & 0 \\ 0 & 0 & 5 \times 10^6 & 0 & 0 & 0 \\ 0 & 0 & 0 & 1 & 0 & 0 \\ 0 & 0 & 0 & 0 & 1 \times 10^7 & 0 \\ 0 & 0 & 0 & 0 & 0 & 1 \times 10^{10} \end{bmatrix}, R_i = 1500 \tag{20}$$

$$K_{LQI} = [256.1 \quad -1602.7 \quad 13.1 \quad 328.9 \quad 51.3 \quad 2582], L_{LQI} = \begin{bmatrix} 410.29 \\ 0.01 \\ 105.91 \\ -0.04 \\ 12.31 \end{bmatrix} \tag{21}$$

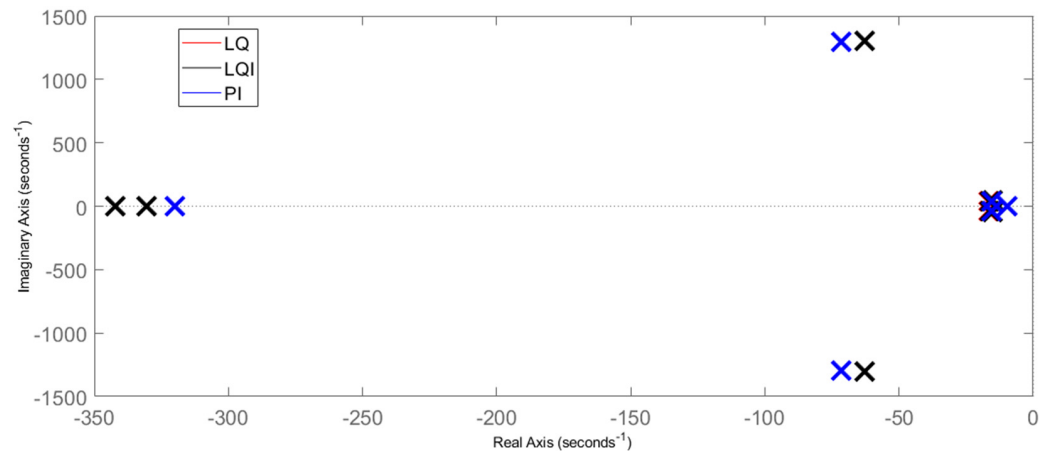


Figure 7. Closed-loop system poles associated with all controllers.

In addition, the low-frequency resonance, attained from complex poles $-2.65 \pm j 108$, is also successfully eliminated by all controllers. Therefore, all the developed controllers can stabilize the closed-loop system since they have successfully eliminated the 0 and $-2.65 \pm j 108$ poles. Figure 8 shows the dominant poles in Figure 7. A subtle difference exists between *LQ* and *LQI* poles, although the same *Q*, *R* values are employed for both. This difference results from tuning the additional factor in the diagonal matrix *Qi*. Moreover, *LQI* has an additional pole on the real axis (i.e., without a complex conjugate part), representing the integrator action effect. Therefore, the poles related to the integrator action of both *PI* and *LQI* are located approximately at the same location. Therefore, the two underdamped poles of the *PI*-controlled system are placed as near as possible to other poles of *LQ* and *LQI* in order to obtain a comparable dynamic response. However, *PI* poles cannot be placed arbitrarily in the space (i.e., they could not be placed closer to *LQ* or *LQI* poles, no matter how many more tuning iterations are performed). This result confirms the same conclusion in [10,14] that *PI* controller is more constrained than *SS* controllers.

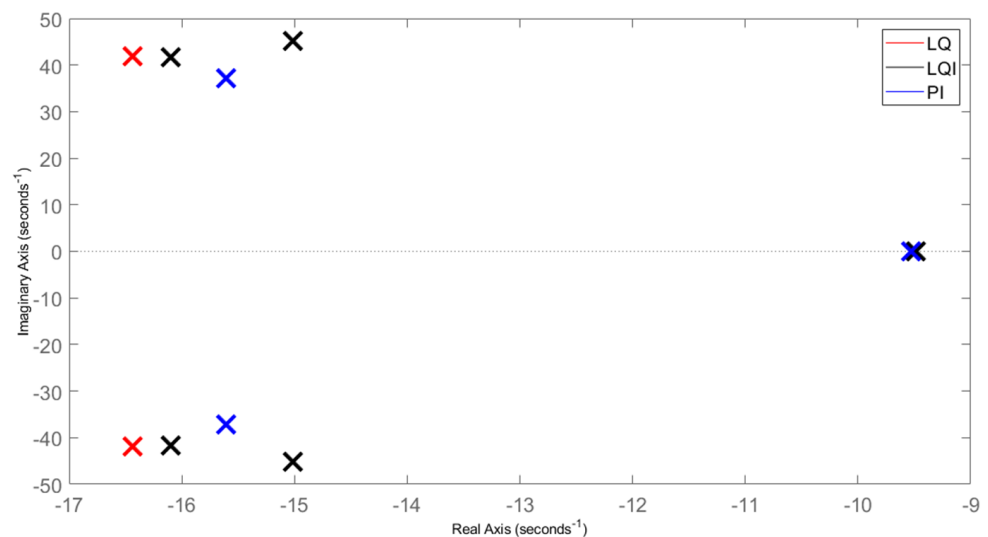


Figure 8. Closed-loop system dominant poles associated with all controllers.

3.2. Frequency Analysis

In Equation (22), the sensitivity function is a simple measure for disturbance attenuation. It indicates how the variations in the output will be affected by feedback. Disturbances with frequencies that make the magnitude of the sensitivity transfer function less than one, i.e., $|S(j\omega)| < 1$, are attenuated. In contrast, disturbances with frequencies such as $|S(j\omega)| > 1$ are amplified by closed-loop. The maximum sensitivity $M_{S_{\sigma}}$, which occurs at

the crossover frequency, is a measure of the most significant amplification of the disturbances. The maximum magnitude of $1/(1 + H(s))$, where $H(s)$ is the open-loop transfer function, is indeed the stability margin. Thus, M_{Sv} is a robustness criterion [10,36]. If M_{Sv} is less than two, the associate closed-loop has good robustness, whereas when M_{Sv} is greater than four, both the robustness and performance would be poor [10].

$$M_{Sv} = \max_{\omega} \left| \frac{1}{1 + H(s)} \right| = \max_{\omega} |S(j\omega)| \tag{22}$$

3.2.1. Stability Analysis

The sensitivity of different closed-loop control systems will be evaluated with and without delay quantities: delay from the electrical part of VEL (i.e., represented by the transfer function G_t) and delay from the angular speed sensor (i.e., represented by the transfer function M). Then, the stability will be evaluated using *Nyquist criteria* [35,36].

The parameters of the total delay transfer function (G_{Δ}) are set according to [10], so that α_t is 1800 rad/s, and T_d equals 0.2 ms. Since T_m depends on the sampling time of the measurement sensor [10,32], it will vary during this work. However, it will be fixed to 0.7 ms in this section. As a result, G_{Δ} can be described as a first-order system with a total delay time of 0.9 ms. The open-loop transfer functions of *PI*, *LQ*, and *LQI* are determined through Equations (23)–(25), respectively

$$H_{PI}(s) = G(s) \left[k_p + \frac{k_i}{s} \right] \tag{23}$$

$$H_{LQ}(s) = K_{LQ}(sI - A + L_{LQ}C)^{-1} + [L_{LQ}G(s) + B_M] \tag{24}$$

$$H_{LQI}(s) = K_x(sI - A + L_{LQI}C)^{-1} + [L_{LQI}G(s) + B_M] + \frac{K_f}{s}G(s). \tag{25}$$

The Nyquist plot in Figure 9 shows that the *PI* closed-loop control system has high robustness with $M_{Sv} = 1$ in the ideal case (i.e., $G_{\Delta} = 1$), while it shows unsatisfactory robustness of $M_{Sv} > 2$ in the presence of a 0.9 ms delay. The Nyquist contour is very close to the -1 point, explaining the low robustness evaluation. Nonetheless, according to Nyquist stability criteria, the closed-loop with the *PI* controller is stable.

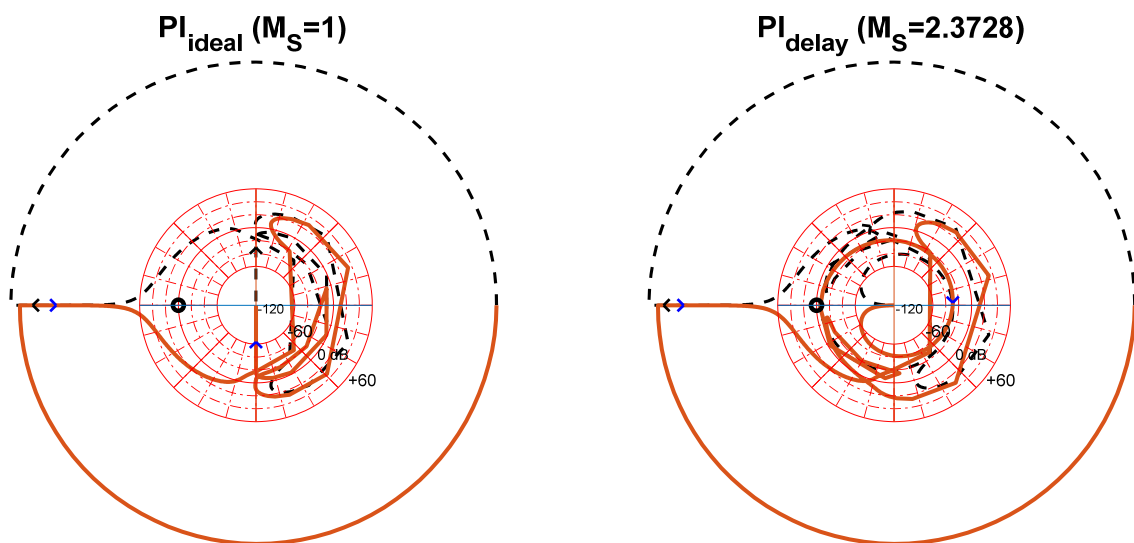


Figure 9. Nyquist plot in logarithmic scale [38] for *PI*-controlled system.

The maximum sensitivity of the LQ closed-loop control system has insignificantly increased due to a time delay, as illustrated in Figure 10. Therefore, according to Nyquist stability criteria, the closed-loop with an LQ controller is stable and robust.

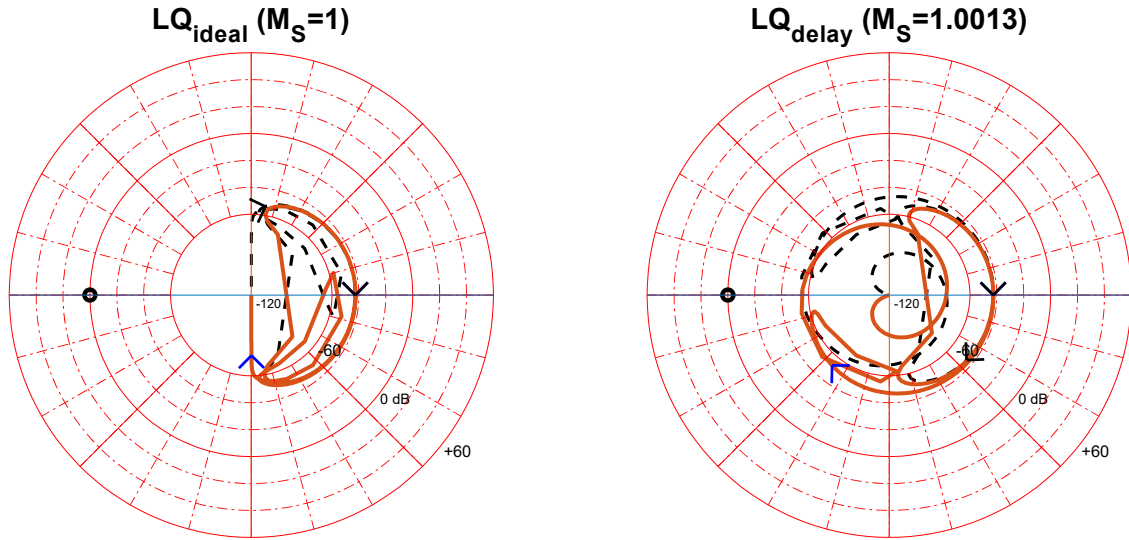


Figure 10. Nyquist plot in logarithmic scale for LQ-controlled system.

In Figure 11, the robustness of the LQI-controlled system provides the same M_{Sv} evaluation as the LQ controller in both cases. In the ideal case, it is worth noting that the LQ and LQI have almost identical Nyquist plots. Also, in case of a time delay, both controllers produced the same outer contour, but the inner contour of LQI forms a spiral pattern. Therefore, according to Nyquist stability criteria, the closed-loop of LQI is stable and robust.

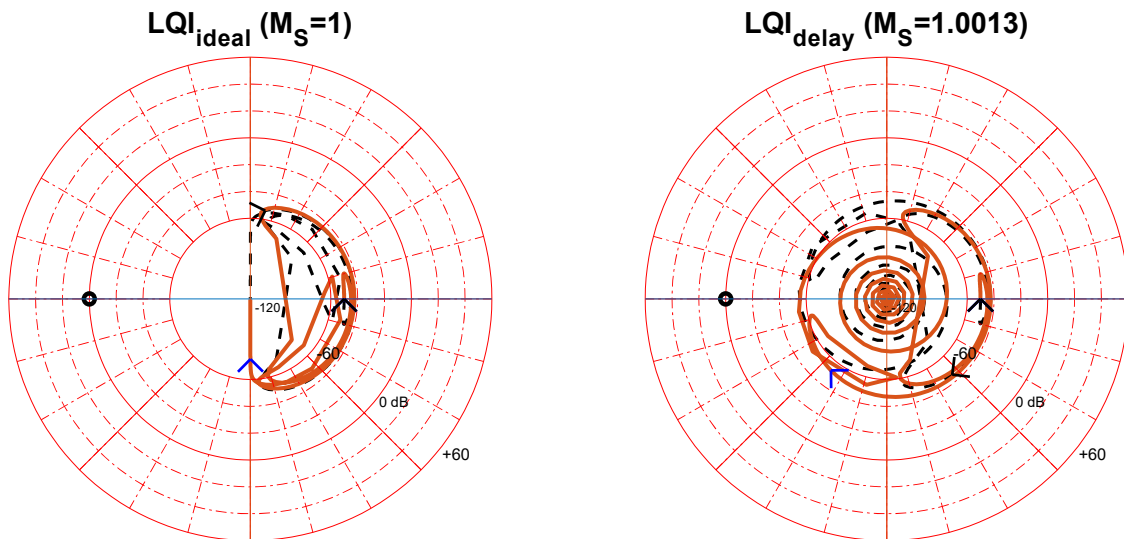


Figure 11. Nyquist plot in logarithmic scale for LQI-controlled system.

3.2.2. Measurement Noise Amplification

The noise amplification of the closed-loop-controlled system is evaluated by the noise transfer function from noise n , shown in Figures 5 and 6, to the electromagnetic motor moment M_M [10]. The noise transfer functions of PI, LQ, and LQI are determined through Equations (26)–(28), respectively. Figure 12 shows the noise rejection for each

controller command moment (i.e., demanded moment by the controller from the electrical loading machine).

$$N_{PI}(s) = -G_t(s) \left[k_p + \frac{k_i}{s} \right] \tag{26}$$

$$N_{LQ}(s) = -G_t(s) \left[\mathbf{K}_{LQ}(s\mathbf{I} - \mathbf{A})^{-1} \mathbf{L}_{LQ} \right] \tag{27}$$

$$N_{LQI}(s) = -G_t(s) \left[\mathbf{K}_{LQI}(s\mathbf{I} - \mathbf{A})^{-1} \mathbf{L}_{LQI} + \frac{K_{\xi}}{s} \right] \tag{28}$$

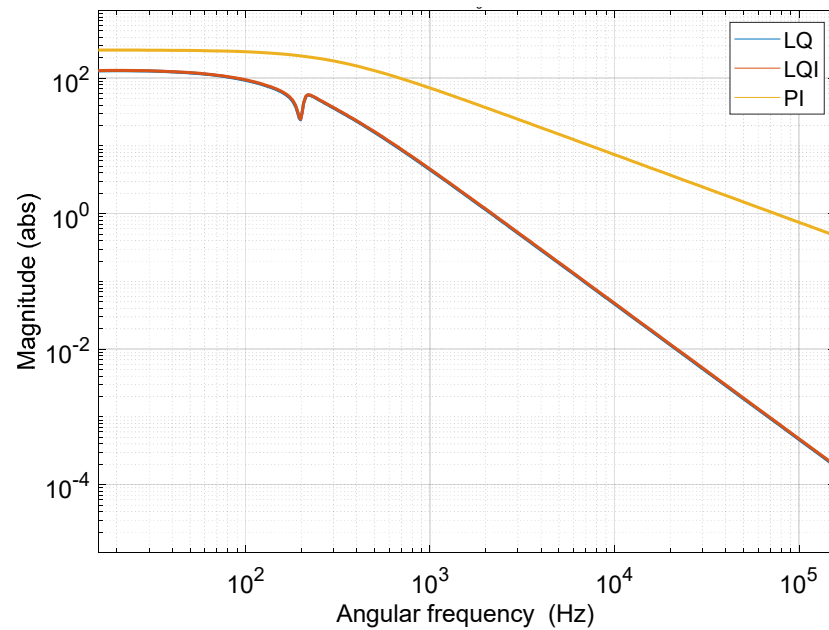


Figure 12. Measurement noise amplification magnitude of all types of controllers with time delay.

Apparently, the noise rejection quality increases with the frequency for each control loop. Moreover, the *LQI* has equivalent characteristics to *LQ*, even in the noise rejection quality. It can also be seen that the *PI* controller provides the worst noise rejection evaluation. The spiral Nyquist form, which results from an internal delay, reflects that high phases offset high frequencies [39]. This means that the phase of the *LQ*-controlled system is the least sensitive to time delay. After evaluating using frequency response analysis, the earlier conclusions will be approved with the time-domain simulation.

4. Simulation Results

In Figure 13, the middle figure shows the desired angular speed, as attained by integrating the angular acceleration signal [10]. The advantage of using this approach is to smoothen the sharp transition angles in the speed profile. In doing so, the high peaks in the system’s acceleration, which may cause high moment impulses, are avoided. The test is highly dynamic due to the abrupt change in angular acceleration 0–1000 rpm (104.7 rad/s) in 0.4 s, equivalent to an acceleration of 9.3 m/s² to the A-Class test vehicle. The simulated powertrain moment at the wheel-hub will be inverted from 500 to –500 N.m after 4 s. The controllers perceive the final powertrain moment as a disturbance moment. This maneuver will show how effectively each controller would respond to maintain the desired speed in high acceleration and disturbance moment demands.

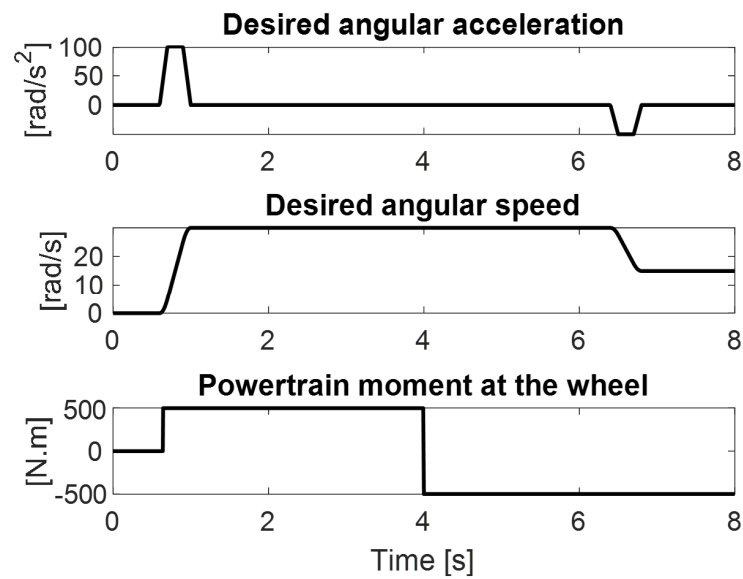


Figure 13. Desired reference signal and powertrain moment.

4.1. Time-Domain Analysis

In Figure 14, the figures at the left show the high robustness of the PI-controlled system with the time delay ignored (i.e., in the ideal case, $G_{\Delta} = 1$). The response also showed an excellent tracking performance. Nevertheless, when a 0.9 ms time delay exists, the PI controller begins to perform poorly after the powertrain moment value is inverted, as shown in the figures at the right. This outcome confirms the accuracy of the frequency analysis. The LQ-controlled system displays high robustness even with a time delay, as shown in Figure 15. However, its time response has a steady-state deviation and no significant influence of a 0.9 ms delay on the system.

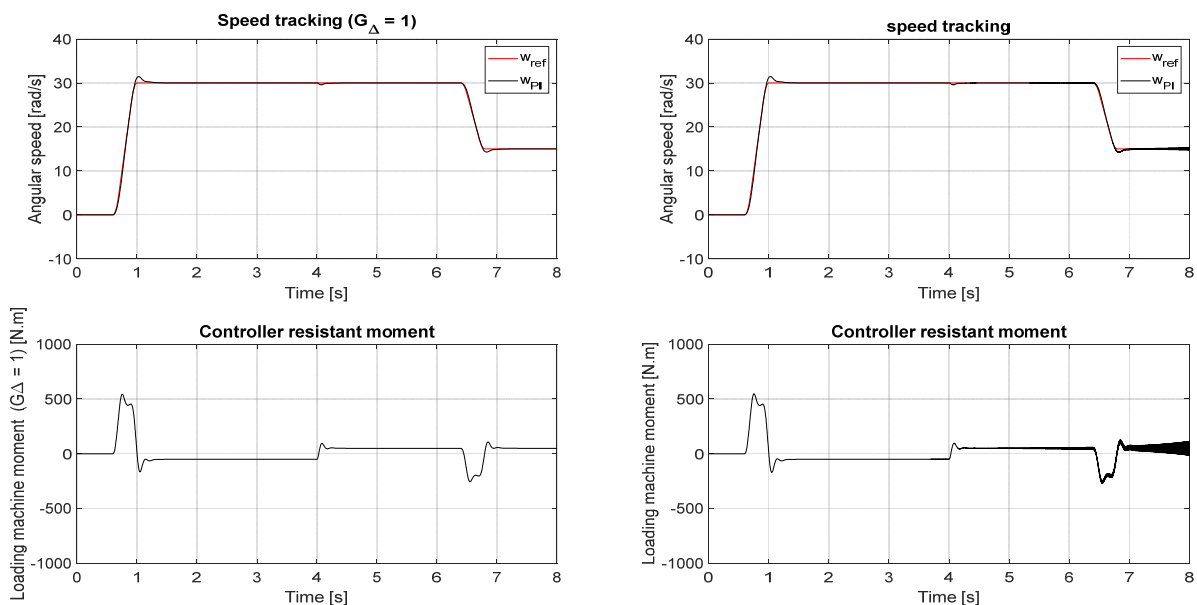


Figure 14. Time response of the PI-controlled system: (Left) without time delay, (Right) with time delay.

Figure 16 shows that the LQI-controlled system has the best tracking performance with zero steady-state error and an insignificant influence of a 0.9 ms delay on the system. Figure 17 presents each controller’s angular speed tracking error in case of a time delay. The PI controller has an analogous tracking response since the dominant poles of PI were

placed close to the dominant poles of LQI. However, the difference in robustness is apparent. Although the LQ controller is robust, it has an absolute steady-state error of 0.37 rad/s. This error occurs as a consequence of applying the powertrain moment. LQI controller, in contrast, demonstrates both high robustness and tracking performance, and it could achieve a zero steady-state error in a short time.

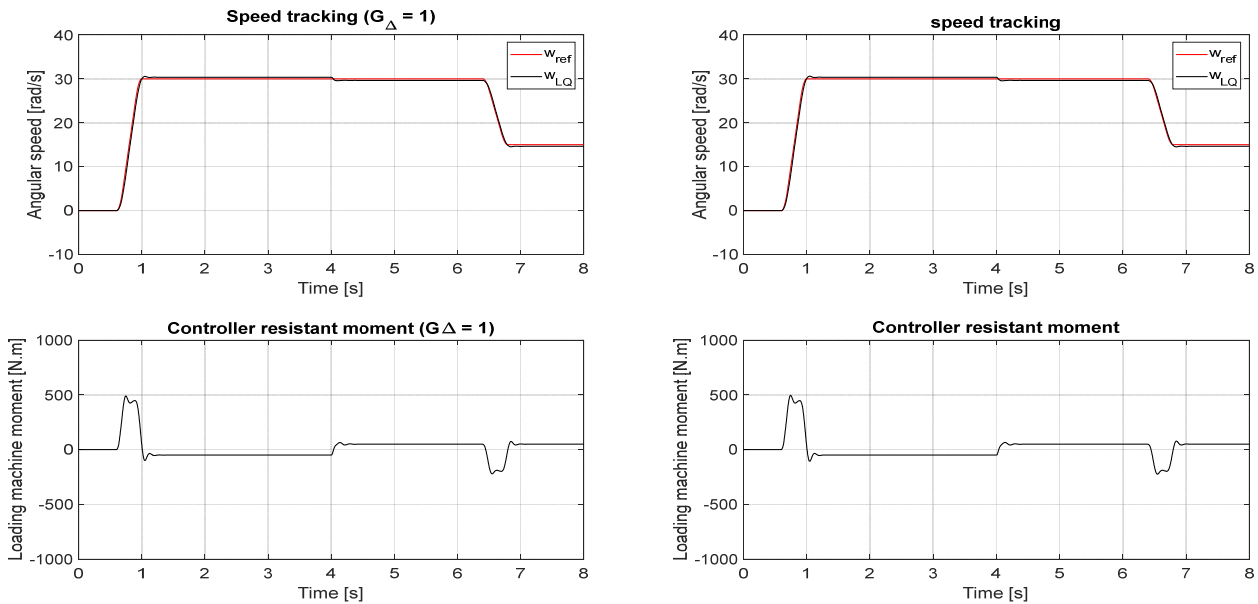


Figure 15. Time response of the optimal LQ-controlled system: (Left) without time delay, (Right) with time delay.

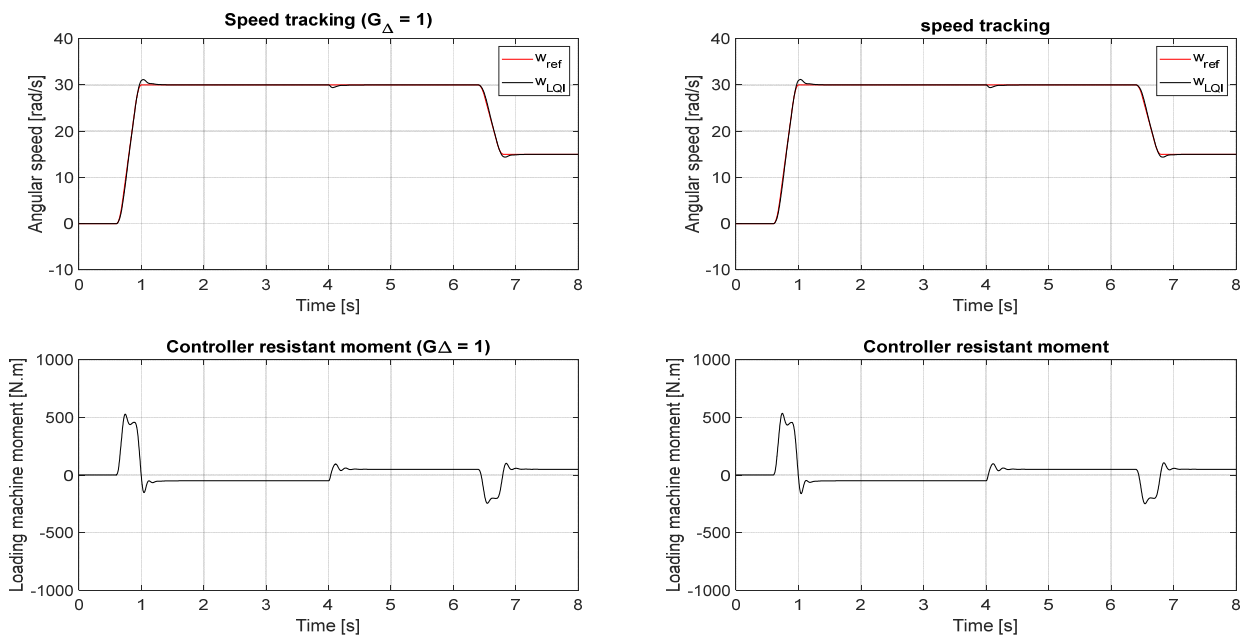


Figure 16. Time response of the optimal LQI-controlled system: (Left) without time delay, (Right) with time delay.

In order to confirm the accuracy of the estimated noise rejection performance, demonstrated in Figure 12, the previous simulation test is executed again. However, this time, white measurement noise is added to the angular speed feedback signal. The previous simulation test is executed again, but this time, white measurement noise is added to the angular speed feedback signal. The white noise has an amplitude of ± 0.5 rad/s and a

sampling time of 1×10^{-5} s. The noise amplification magnitudes for PI, LQ, and LQI are 4.6778, 0.01878, and 0.01832, respectively. So, the control command is expected to have high noise amplification when the PI controller is implemented. In contrast, LQ and LQI should handle the measurement noise with low influence in the control signal. These expectations are proven in Figures 18–20.

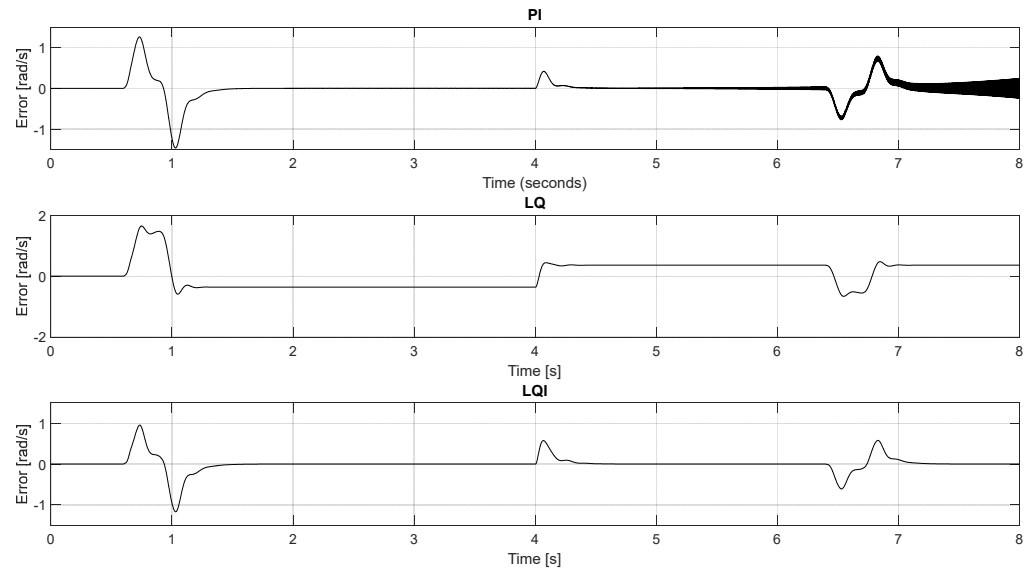


Figure 17. Influence of the time delay on the angular speed error: (Top) PI-controlled, (Middle) LQ-controlled, (Bottom) LQI-controlled.

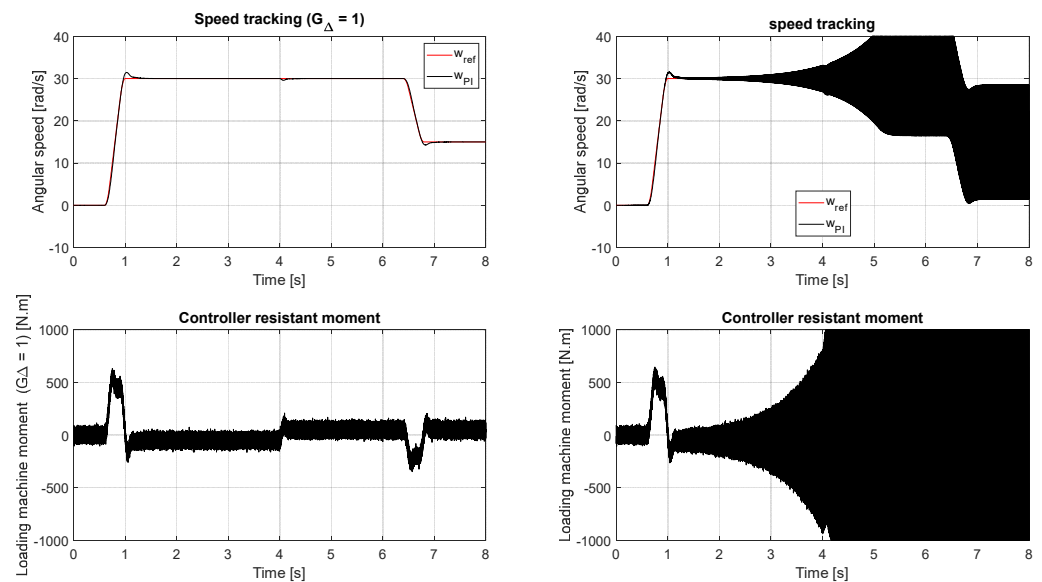


Figure 18. Measurement noise amplification of PI controller: (Left) without time delay, (Right) with time delay.

The simulation results meet the expectations of the noise model, where the PI controller leads to high noise amplification that causes noise in the controller moment that exceeds ± 1000 N.m, compared to the case of the noise-free measurements. Moreover, with both time delay and noise, the PI controller drove the system to instability directly after attempting to settle the angular speed to 30 rad/s. On the contrary, both LQ and LQI controllers had a low noise of ± 3 N.m in the controller signal.

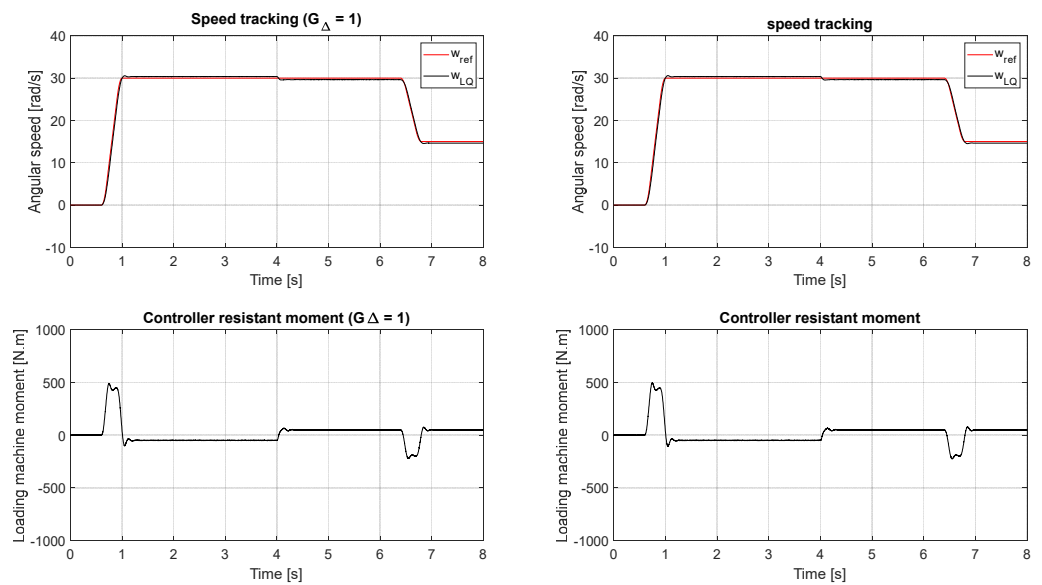


Figure 19. Measurement noise amplification of LQ controller: (Left) without time delay, (Right) with time delay.

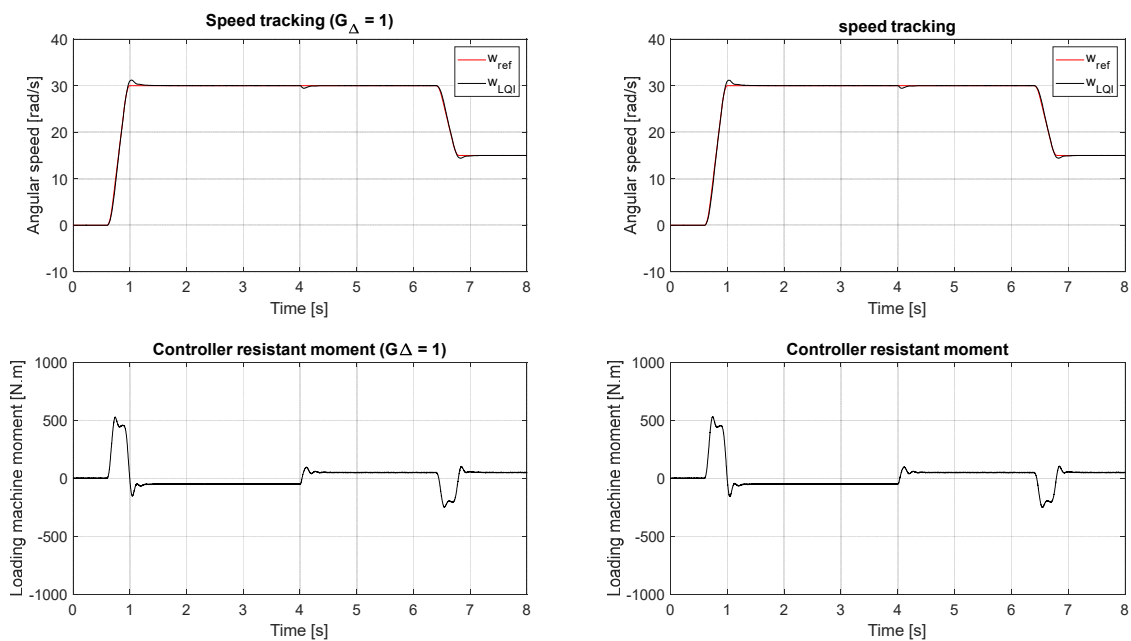


Figure 20. Measurement noise amplification of LQI controller: (Left) without time delay, (Right) with time delay.

In summary, the PI controller has fewer closed-loop poles than both LQ and LQI controllers, making it less efficient in controlling complex systems. LQ and LQI demonstrate high robustness against a time delay and measurement noise. PI, conversely, could not handle highly dynamic reference signals in the presence of time delay. In addition, PI has bad noise rejection quality compared to both LQ and LQI. Based on these results, the PI controller option will not be considered for further testing in the rest of this work.

4.2. Sensitivity Analysis for a Single Parameter Uncertainty

The selected controllers are designed based on prior knowledge of system model equations and the values of their parameters. The concept of uncertainty will be employed by repeating the same tests several times. Each test will be conducted with a new variation

in a specific parameter. Only LQ and LQI will be investigated. No further analysis will be made for PI since it failed the basic tests. In this section, the sensitivity of each controlled system will be examined concerning time delay sensitivity, disturbance moment effect, single parameters uncertainty, and multiparameter uncertainty. Previously, the time delay sources were introduced: the test bench electrical components delay, which resembled the G_t function model (4), and the measurements time delay expressed in Equation (5). The test is performed with a fixed T_d at 0.2 s, and T_m varies randomly in the range of [0.5, 5] ms. LQ proved highly robust against T_m , apart from speed tracking efficiency, as shown in Figure 21. However, as expected from the frequency analysis section, LQI is more sensitive to time delay than LQ, as demonstrated in Figure 22. Still, LQI could handle measurement time delay variations until 5 ms.

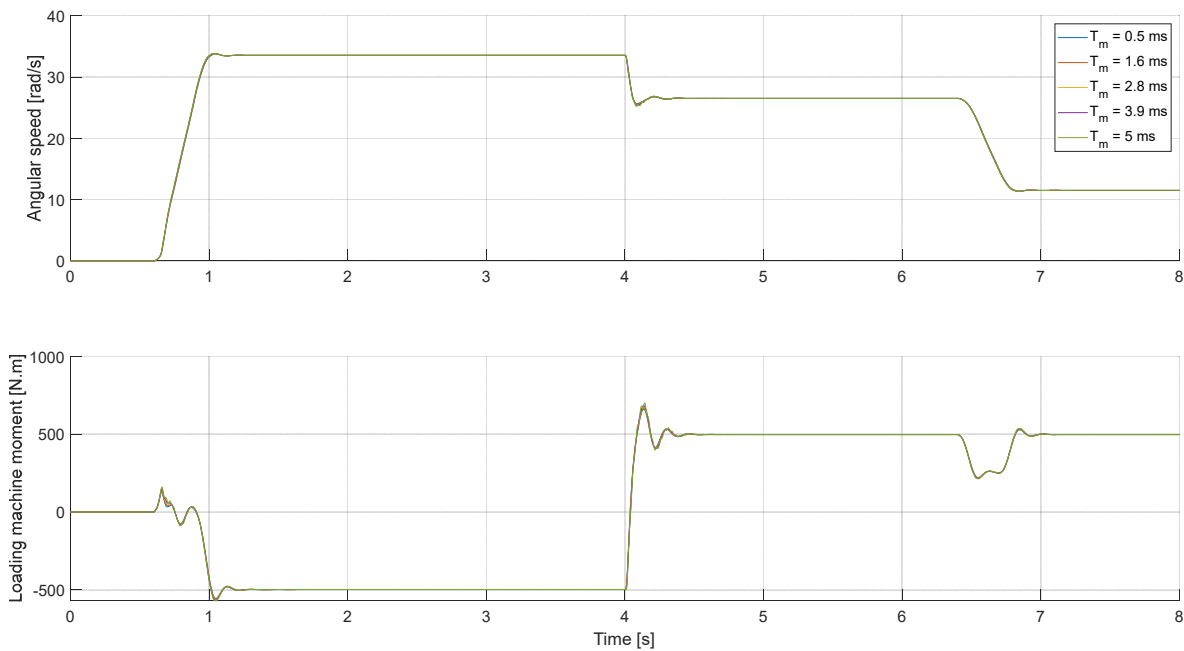


Figure 21. Time response of LQ-controlled system at different T_m values.

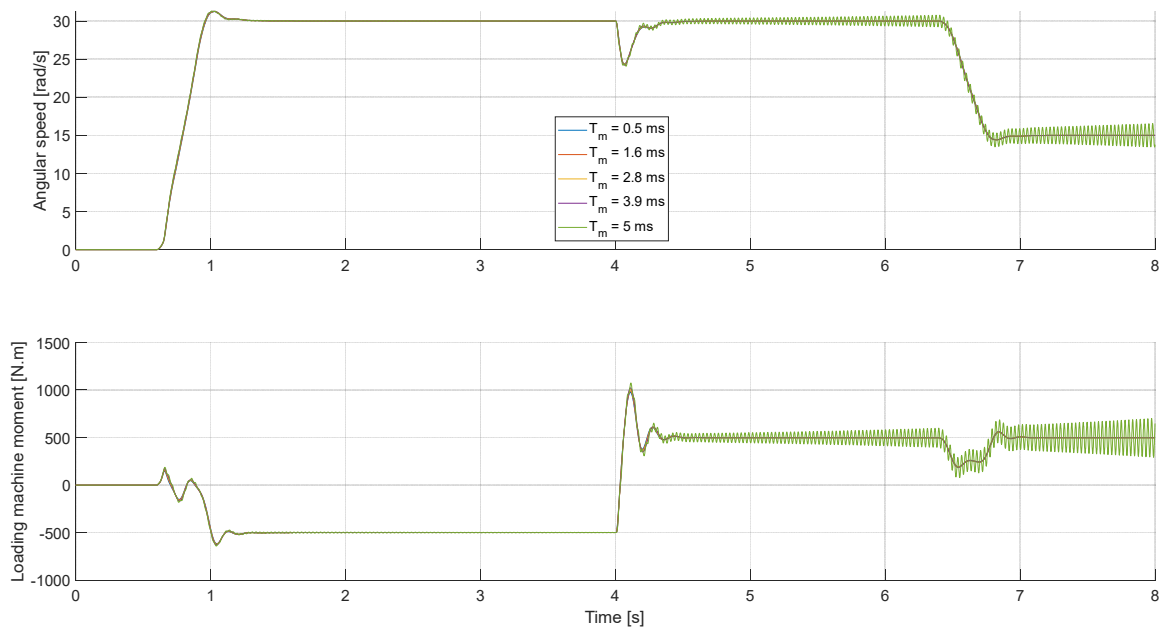


Figure 22. Time response of LQI-controlled system at different T_m values.

The electrical loading machine perceives the powertrain driving moment (M_{drive}) as a disturbance moment. Therefore, the loading machine should generate a resistance moment according to the desired rotational speed value. Figures 23 and 24 illustrate the influence of changing the driving moment on LQ- and LQI-controlled systems, respectively. At no load testing (i.e., $M_{drive} = 0$ N.m), LQ followed the desired speed profile perfectly. However, there will be a consequent shift in LQ speed response with any moment applied. Positive moment values (i.e., driving moment) lead to an upward offset in LQ speed response. In comparison, a negative or braking moment causes a downward offset. In contrast, LQI maintained the same speed response at all disturbance moment values. Also, it was able to compensate for the extreme moment change. For instance, when changes were made from 500 to -500 N.m, the result was an error of 5 rad/s. This error was corrected in about 0.5 s. Therefore, the same LQ- and LQI-tuned parameters will be used for all tests to study the influence of parameter uncertainties on controllers' performance. Furthermore, a large disturbance moment (500 to -500 N.m) is applied to put the controllers under extreme conditions. Figure 25 illustrates the influence of uncertainty in J_{Pt2W} , where the Monte Carlo simulation is utilized to generate random variations in J_{Pt2W} . The LQ controller proved to be highly robust against uncertain J_{Pt2W} values. At the same time, no significant change in both angular speed tracking and controller command response is observed.

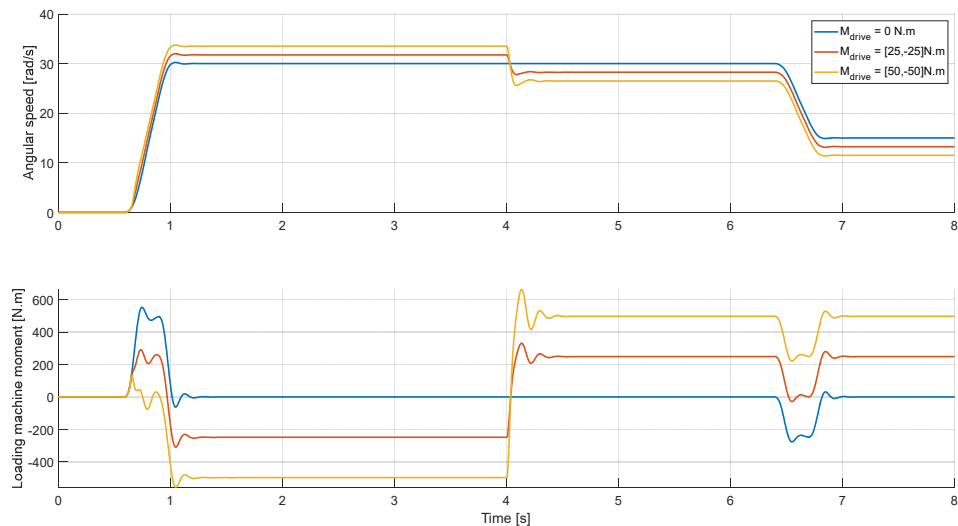


Figure 23. Time response of LQ-controlled system at different M_{drive} values.

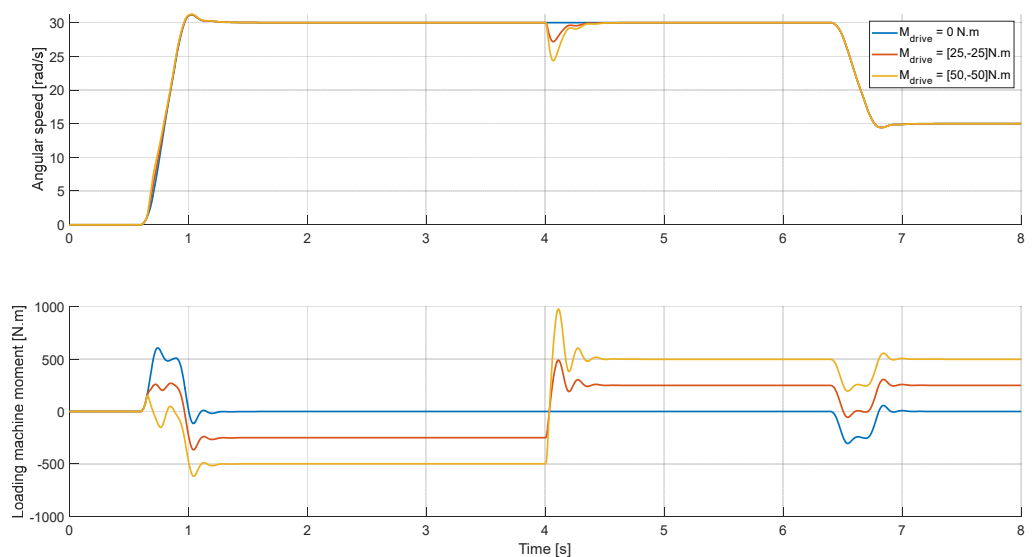


Figure 24. Time response of LQI-controlled system at different M_{drive} values.

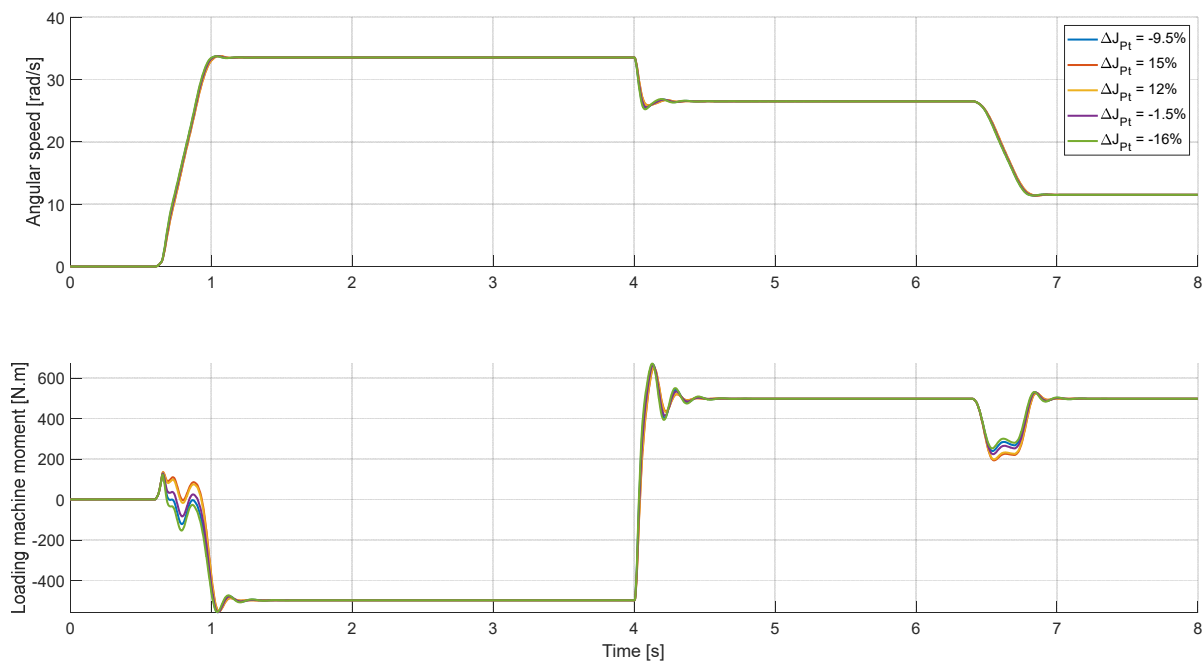


Figure 25. Time response of LQ-controlled system at different J_{Pt2W} values.

Also, Figure 26 displays that the LQI controller maintained high tracking performance against uncertain J_{Pt2W} values and the controller’s moment command, which was slightly influenced. The same technique is also employed to investigate the effect of K_{Ax} uncertainty. Uncertain K_{Ax} estimation caused no substantial alteration in LQ controller performance, as in Figure 27. Despite this, the angular speed and moment did not reach the same steady-state values in all cases. Likewise, the LQI controller could sustain the uncertainty of K_{Ax} and provide nearly unchanged angular speed tracking performance despite the considerable variations in K_{Ax} . The results are shown in Figure 28.

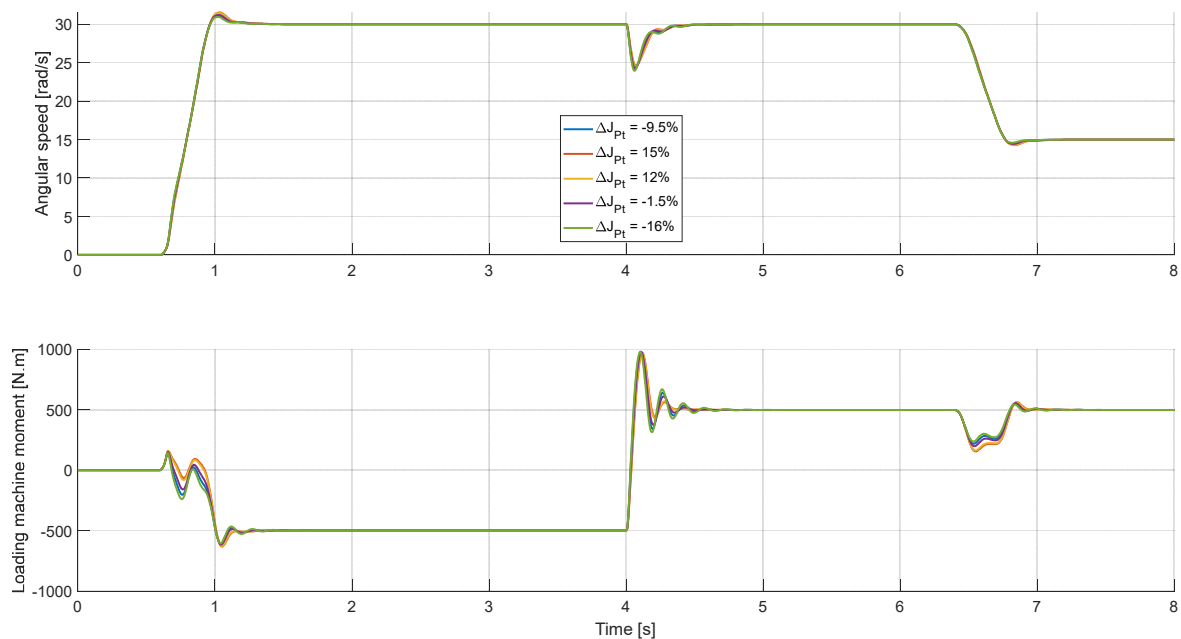


Figure 26. Time response of LQI-controlled system at different J_{Pt2W} values.

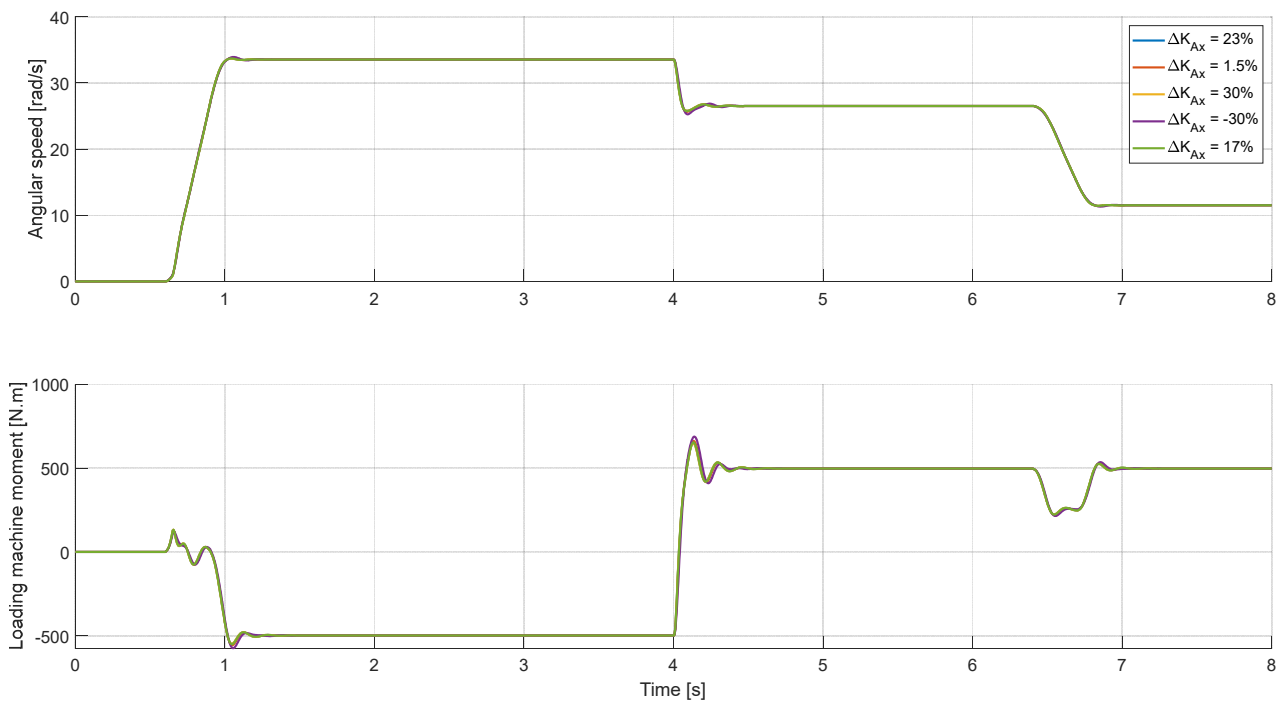


Figure 27. Time response of LQ-controlled system at different K_{Ax} values.

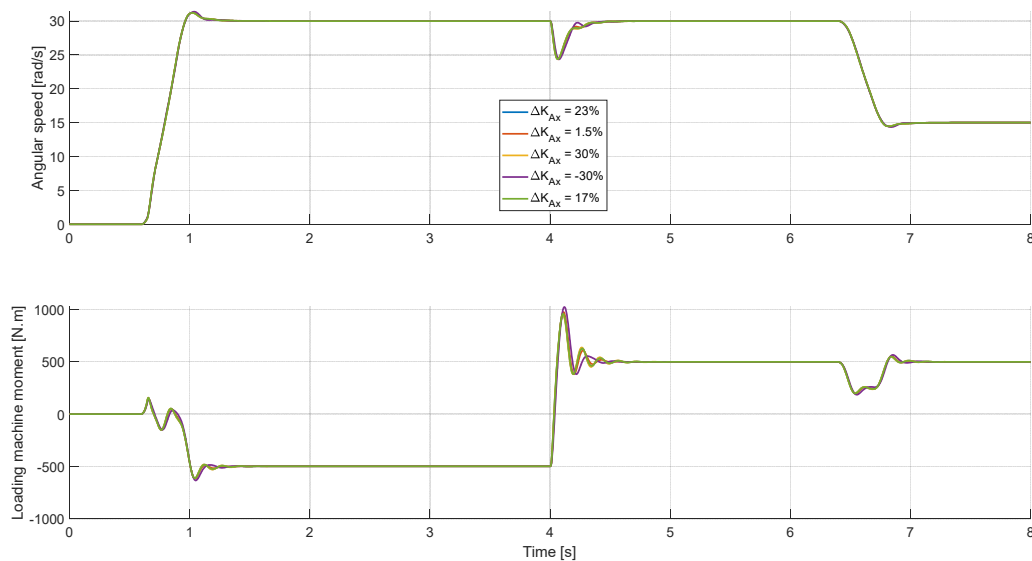


Figure 28. Time response of LQI-controlled system at different values.

4.3. Sensitivity Analysis for Multiple Parameter Uncertainties

The same uncertain value variations of J_{P12W} and K_{Ax} are combined in pairs. The results for LQ- and LQI-controlled systems are presented in Figures 29 and 30, respectively. Obviously, with two incorrect parameter estimations, the speed response of LQ changed substantially. In comparison, the LQI has preserved almost the same tracking response with minor variations. It is, however, worth noticing that the moment control command is different in each case. For example, it did not reach ± 500 N.m at a steady state, as when the parametrization was accurate. Moreover, more oscillations appeared in the controller command after each transient state for some tests.

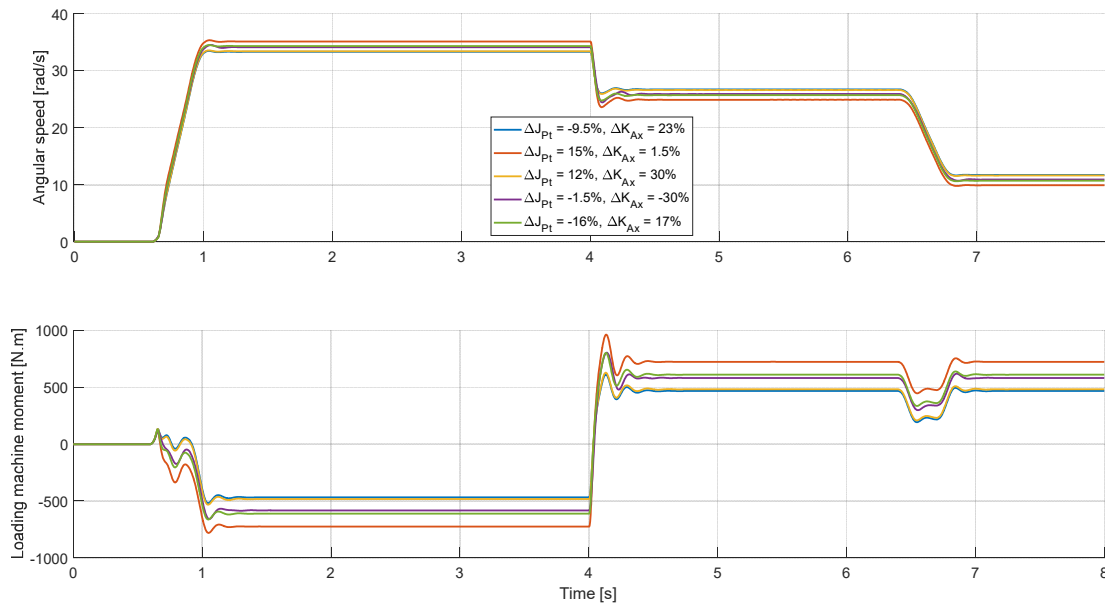


Figure 29. Time response of LQ-controlled system at different J_{Pt2W} and K_{Ax} values.

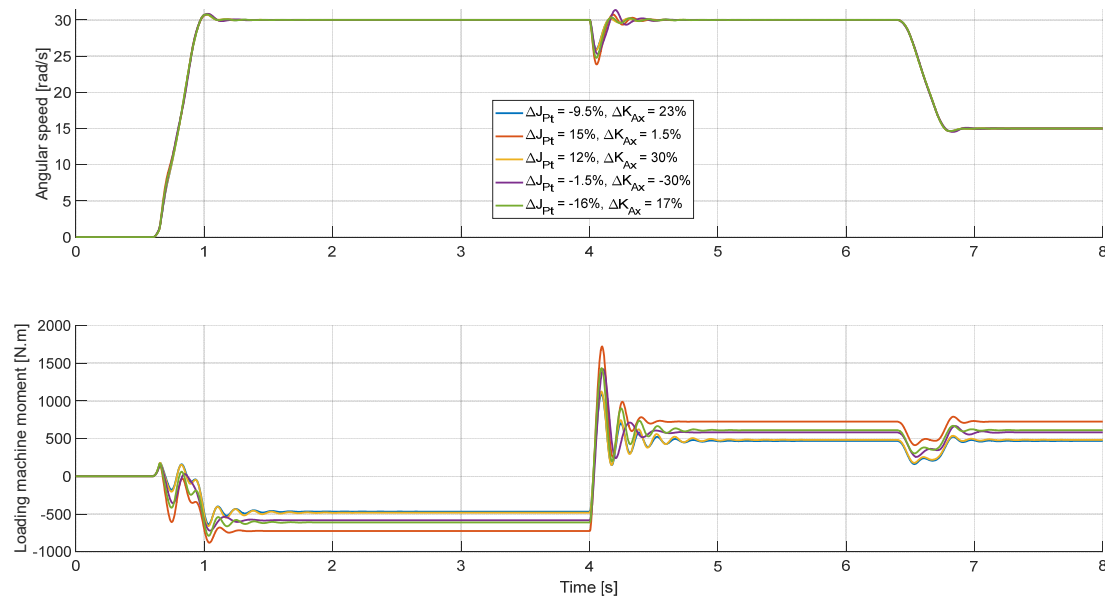


Figure 30. Time response of LQI-controlled system at different J_{Pt2W} and K_{Ax} values.

5. Conclusions

A complete vehicle test bench is examined with the help of simulation models. The complex system from coupling the powertrain of the electric test vehicle with the mechanical part of the test bench is modelled in a three-mass system. It can be concluded that if the same Q and R parameters are employed with fine-tuning of the integral weighting factor in LQI, both LQ, and LQI could achieve the same gain margin. However, there will be a difference in the phase margin due to the integral effect of the LQI controller. Moreover, time delay affects only the system phase in the frequency domain analysis, while it does not influence the frequency gain. In addition, the additional integration in the LQI reduces its phase margin compared to its equivalent LQ-controlled system. However, the speed error in the LQ control increases with the disturbance moment. In contrast, LQI can sustain approximately the same response regardless of the disturbance moment. Ideally, if there is no delay in the system, all controllers suppress the vibrations efficiently. Nevertheless, the PI-controlled system became vulnerable to instability as the time delay was introduced to

the model. In contrast, LQ- and LQI-controlled systems remained stable despite extreme operating conditions. Regarding parameter uncertainty, overestimating the powertrain inertia leads to a lower controller command moment in the transient states but slightly more oscillation in the response. On the other hand, underestimated powertrain inertia forces the controllers to generate higher moments than accurate parametrization. When the axle stiffness is the only uncertain parameter, the impact on LQ and LQI responses is minor. Despite this, LQ did not perform well with uncertainty in both the powertrain inertia and axle stiffness. In contrast, multiparameter uncertainty did not significantly affect LQI performance. However, it did influence the controller effort response.

This work can be extended by developing a moment controller to control the power of the test vehicle mounted on the test bench. As both the speed and moment become controlled variables, the VEL test bench would be beneficial in different development scopes, such as energy consumption estimations and real-world driving scenarios. Furthermore, the performance of nonlinear control algorithms could be compared to the proposed LQI controller. In addition, further optimal control techniques may be investigated.

Author Contributions: M.A. did the literature review, created the simulation model, developed the controllers' algorithms, performed the results analysis, and wrote the paper. F.G. supervised the project work related to this paper. All authors have read and agreed to the published version of the manuscript.

Funding: The KIT-Publication Fund of the Karlsruhe Institute of Technology funded this publication.

Institutional Review Board Statement: Not applicable.

Informed Consent Statement: Not applicable.

Data Availability Statement: The data presented in this study are openly available in FigShare at <https://doi.org/10.6084/m9.figshare.24798516>.

Acknowledgments: Many thanks to Lutz Gröll from the Institute for Automation and Applied Informatics for his outstanding lecture notes, which were the essential inspiration in developing the control algorithms in this work. We also acknowledge support by the KIT-Publication Fund of the Karlsruhe Institute of Technology.

Conflicts of Interest: The authors declare no conflict of interest.

Abbreviations

Symbol	Description
CV	Constant velocity shaft
D_{Ax}	Axle internal damping
D_S	CV shaft internal damping
H	Open-loop transfer function
i_d	Differential gear ratio
i_g	Transmission gear ratio
I-SS	State-space with integral action
J_E	Vehicle electric motor inertia
J_G	Gearbox inertia
J_M	Electric machine inertia
J_{Pt2W}	Front axle inertia plus half of the powertrain equivalent inertia
J_S	Shaft inertia around its longitudinal axis
J_T	Equivalent inertia of the electrical loading machine and the continuous velocity shaft
J_W	Wheel-hub inertia
$k_{\Delta\omega}$	Viscous friction factor
K_{Ax}	Axle stiffness
k_i	Integral gain
K_{LQ}	Full-state feedback gain matrix for the LQ controller
K_{LQI}	Full-state feedback gain matrix for the LQI controller

k_M	Friction moment factor
k_p	Proportional gain
K_s	Shaft equivalent rotational stiffness
L_{LQ}	Luenberger observer gain matrix for LQ controller
L_{LQI}	Luenberger observer gain matrix for LQI controller
LQ	Linear-quadratic
LQI	Linear-quadratic with integral action
$M(s)$	Measurement time delay transfer function
M_{drive}	Total powertrain driving moment
M_e	Electric motor moment
M_F	Coulomb friction moment
M_M	Electrical loading machine moment
MPC	Model predictive control
M_{Sv}	Maximum sensitivity
M_{Sx}	Final output moment at one side of the differential gear
PI	Proportional-integral-controller
PI-SS	PI with state-space feedbacks
S	Sensitivity transfer function
SS	State-space
T_d	Time delay in the moment control loop
T_m	Measurement time delay
VEL	VEHICLE-in-the-Loop
VHiL	Vehicle-in-the-loop
VUT	Vehicle under test
y	Measured system's output
y_d	Reference input for the controller
$\Delta\omega_D$	Angular speed difference between the differential gear outputs
θ_D	The differential gear output angular position
θ_M	The loading machine angular position
θ_{Sx}	Angular position of the differential gear output
θ_W	the wheel-hub angular position
ω_M	Motor angular speed
ω_{Sx}	Angular speed of the differential gear output
ω_W	Wheel rotational speed

References

- Bauer, R. Neues Regelkonzept für die dynamische Antriebsstrangprüfen. In *17. Steirisches Seminar Über Regelungs-Technik und Prozessautomatisierung*; Graz University of Technology: Graz, Austria, 2011; pp. 104–116.
- Bauer, R. *New Methodology for Dynamic Drive Train Testing*; SAE Technical Papers; SAE International: Warrendale, PA, USA, 2011; pp. 1–6.
- Nehlsen, M.; Jedicke, F.; Bogner, E.; Schöggel, P. Fahrbarkeitsuntersuchungen auf dem rollenprüfstand. *ATZ Automob. Z.* **2006**, *108*, 376–381. [[CrossRef](#)]
- Weber, S.; Dursun, Y.; Kirschbaum, F.; Jakobi, R.; Bäker, B.; Fischer, J. Investigations of the process of road matching on powertrain test rigs. In *Internationales Stuttgarter Symposium*; Springer: Stuttgart, Germany, 2017; pp. 1247–1261.
- Schenk, J. Prüfplattform Für Mechatronisch Ausgestattete Fahrzeuge in Entwicklung und Produktion. 2007. Available online: http://publications.rwth-aachen.de/record/49934/files/Schenk_Jan.pdf (accessed on 16 November 2022).
- Nordin, M.; Gutman, P.O. Controlling mechanical systems with backlash—A survey. *Automatica* **2002**, *38*, 1633–1649. [[CrossRef](#)]
- Fietzek, R.; Rinderknecht, S. Car-in-the-Loop Complete Vehicle Test Rig. *SAE Int. J. Passeng. Cars-Mech. Syst.* **2015**, *8*, 476–481. [[CrossRef](#)]
- Gröll, L. *Moderne Regelungskonzepte I—Lecture Notes*; Karlsruhe Institute of Technology: Karlsruhe, Germany, 2015.
- Hohmann, S. *Systemdynamik und Regelungstechnik—Lecture Notes*; Karlsruhe Institute of Technology: Karlsruhe, Germany, 2017.
- Saarakkala, S.E.; Hinkkanen, M. State-space speed control of two-mass mechanical systems: Analytical tuning and experimental evaluation. *IEEE Trans. Ind. Appl.* **2014**, *50*, 3428–3437. [[CrossRef](#)]
- Fietzek, R. *Modellbildung, Regelung und Realisierung Eines Neuartigen Konzepts für Einen Gesamtfahrzeugprüfstand*, 1st ed.; Shaker: Albany, NY, USA, 2014.
- Szabat, K.; Orłowska-Kowalska, T. Vibration suppression in a two-mass drive system using PI speed controller and additional feedbacks—Comparative study. *IEEE Trans. Ind. Electron.* **2007**, *54*, 1193–1206. [[CrossRef](#)]

13. Thomsen, S.; Hoffmann, N.; Fuchs, F.W. PI control, PI-based state space control, and model-based predictive control for drive systems with elastically coupled loads—A comparative study. *IEEE Trans. Ind. Electron.* **2011**, *58*, 3647–3657. [[CrossRef](#)]
14. Saarakkala, S.E.; Hinkkanen, M.; Zenger, K. Speed control of two-mass mechanical loads in electric drives. In Proceedings of the 2012 IEEE Energy Conversion Congress and Exposition, ECCE 2012, Raleigh, NC, USA, 15–20 September 2012; pp. 1246–1253.
15. Zhang, G.; Furusho, J. Speed control of two-inertia system by PI/PID control. *IEEE Trans. Ind. Electron.* **2000**, *47*, 603–609. [[CrossRef](#)]
16. Szabat, K.; Orłowska-Kowalska, T. Application of the Kalman filters to the high-performance drive system with elastic coupling. *IEEE Trans. Ind. Electron.* **2012**, *59*, 4226–4235. [[CrossRef](#)]
17. Szabat, K.; Orłowska-Kowalska, T. Adaptive control of two-mass system using nonlinear extended Kalman Filter. In Proceedings of the IECON Proceedings (Industrial Electronics Conference), Paris, France, 6–10 November 2006; pp. 1539–1544.
18. Ji, J.K.; Sul, S.K. Kalman Filter and LQ Based Speed Controller for Torsional Vibration Suppression in a 2-Mass Motor Drive System. *IEEE Trans. Ind. Electron.* **1995**, *42*, 564–571.
19. Beineke, S.; Schuette, F.; Grotstollen, H. Comparison of Methods for State Estimation and Online Identification in Speed and Position Control Loops. 1997. Available online: https://www.semanticscholar.org/paper/COMPARISON-OF-METHODS-FOR-STATE-ESTIMATION-AND-IN-Beineke-Sch%C3%BCtte/afb1259a49ce983090adccafa53f4f1d29e86686?utm_source=direct_link (accessed on 9 November 2023).
20. Zhang, R.; Tong, C. Torsional vibration control of the main drive system of a rolling mill based on an extended state observer and linear quadratic control. *JVC/J. Vib. Control* **2006**, *12*, 313–327. [[CrossRef](#)]
21. El-Haji, M. *Ontologie-Basierte Definition von Anforderungen an Validierungswerkzeuge in der Fahrzeugtechnik*; KIT Scientific Publishing: Karlsruhe, Germany, 2016. [[CrossRef](#)]
22. Pillas, J. *Modellbasierte Optimierung Dynamischer Fahrmanöver Mittels Prüfständen*; Shaker: Albany, NY, USA, 2017. Available online: <https://www.shaker.de/de/content/catalogue/index.asp?lang=de&ID=8&ISBN=978-3-8440-5420-0> (accessed on 16 November 2022).
23. Forstinger, M. *Modelling, Simulation, and Control of Power Train Test Beds*. 2017. Available online: <https://diglib.tugraz.at/download.php?id=5bebd9d691234&location=browse> (accessed on 14 November 2022).
24. Forstinger, M.; Bauer, R.; Hofer, A.; Rossegger, W. Multivariable control of a test bed for differential gears. *Control Eng. Pract.* **2016**, *57*, 18–28. [[CrossRef](#)]
25. Gauterin, F. *Automotive Engineering I—Lecture Notes*; Karlsruhe Institute of Technology: Karlsruhe, Germany, 2017.
26. Gao, Z.; LaClair, T.; Ou, S.; Huff, S.; Wu, G.; Hao, P.; Boriboonsomsin, K.; Barth, M. Evaluation of electric vehicle component performance over eco-driving cycles. *Energy* **2019**, *172*, 823–839. [[CrossRef](#)]
27. Petersen, M.R.; Starkey, J.M. *Nonlinear Vehicle Performance Simulation with Test Correlation and Sensitivity Analysis*; SAE Technical Papers; SAE International: Warrendale, PA, USA, 1996; pp. 643–653.
28. Hu, J.; Peng, T.; Jia, M.; Yang, Y.; Guan, Y. Study on electromechanical coupling characteristics of an integrated electric drive system for electric vehicle. *IEEE Access* **2019**, *7*, 166493–166508. [[CrossRef](#)]
29. Scamarcio, A.; Metzler, M.; Gruber, P.; de Pinto, S.; Sorniotti, A. Comparison of Anti-Jerk Controllers for Electric Vehicles with On-Board Motors. *IEEE Trans. Veh. Technol.* **2020**, *69*, 10681–10699. [[CrossRef](#)]
30. Ineichen, L. *Konzeptvergleich zur Bekämpfung der Torsionsschwingungen im Antriebsstrang Eines Kraftfahrzeugs*; KIT Scientific: Karlsruhe, Germany, 2013. [[CrossRef](#)]
31. Harnefors, L.; Nee, H.P. Model-based current control of ac machines using the internal model control method. *IEEE Trans. Ind. Appl.* **1998**, *34*, 133–141. [[CrossRef](#)]
32. Muszynski, R.; Deskur, J. Damping of torsional vibrations in high-dynamic industrial drives. *IEEE Trans. Ind. Electron.* **2010**, 544–552. [[CrossRef](#)]
33. Fietzek, R.; Rinderknecht, S. Observer validation and model based control of a two mass oscillator with backlash. In Proceedings of the IEEE International Conference on Mechatronics and Automation (IEEE ICMA 2013), Takamatsu, Japan, 4–7 August 2013. [[CrossRef](#)]
34. Thomsen, S.; Fuchs, F.W. Speed control of torsional drive systems with backlash. In Proceedings of the 13th European Conference on Power Electronics and Applications (EPE '09), Barcelona, Spain, 8–10 September 2009; pp. 1–10.
35. Ogata, K. *Modern Control Engineering*, 5th ed.; Prentice Hall: London, UK, 2009.
36. Astrom, K.J.; Murray, R.M. *Feedback Systems—An Introduction for Scientists and Engineers*; Princeton University Press: London, UK, 2010.
37. Orłowska-Kowalska, T.; Szabat, K. Neural-Network application for mechanical variables estimation of a two-mass drive system. *IEEE Trans. Ind. Electron.* **2007**, *54*, 1352–1364. [[CrossRef](#)]

38. Ballotta, L. Complete Nyquist Plot on Logarithmic Scale. 2021. Available online: <https://github.com/lucaballotta/NyquistLog> (accessed on 8 November 2023).
39. Segovia, V.R.; Hägglund, T.; Åström, K.J. Measurement noise filtering for PID controllers. *J. Process Control* **2014**, *24*, 299–313. [[CrossRef](#)]

Disclaimer/Publisher’s Note: The statements, opinions and data contained in all publications are solely those of the individual author(s) and contributor(s) and not of MDPI and/or the editor(s). MDPI and/or the editor(s) disclaim responsibility for any injury to people or property resulting from any ideas, methods, instructions or products referred to in the content.